Design and Development of Cr-Si Based Intermetallic Alloys

Amir Nanpazi

A thesis submitted for the degree of Doctor of Philosophy

Department of Materials Science and Engineering

The University of Sheffield

March 2015

“Let the beauty of what you love be what you do.”

Rumi (1207-1273 A.D.)

Abstract

The motivation for the research described in this thesis was to study the oxidation behaviour of Cr rich Al and Si containing alloys with low transition metal additions as potential bond coat alloys for a coating system for ultra-high refractory metal silicide based alloys. The thesis is an experimental study of the microstructures of cast and heat-treated ternary Cr-Si-Al-M alloys with Al/Si ratios of 0.1 and 1 and individual additions of 5 at.% M = Hf, Nb and Ti and of the isothermal oxidation of the cast alloys at 800, 1000 and 1200 ^{o}C. A brief review of relevant literature is given. The experimental techniques used in the research, namely DSC, X-ray diffraction (Bragg–Brentano and glancing angle), EBSD, TG, SEM and EDS are described. The isothermal heat treatment of the alloys was carried out under argon at 1200 and 1300 ^{o}C for 100 hours.

In the cast alloys with Al/Si = 0.1 the M_6Si_5 type intermetallics and the Cr_5Si_3 and $CrSi_2$ silicides were formed but not the CrSi, which was formed after heat treatment at 1300 ^{o}C in the alloy with M = Ti. The 6-5 intermetallics exhibited no solubility for Al and in the Cr silicides the solubility of Al depended on silicide type and alloying addition M and was highest in both Cr silicides in the alloy with M = Nb. The volume fractions of M_6Si_5 were the highest in each of the alloys with M = Ti and Hf where the lowest fractions were for the Cr_5Si_3 and $CrSi_2$ respectively. In the alloy with M = Nb the disilicide had the lowest fraction and the 5-3 silicide the highest.

None of the alloys with Al/Si = 0.1 exhibited pest oxidation. The alloy with M = Nb had the highest weight gains at each oxidation temperature. At 800 and 1200 ^{o}C the alloy with M = Ti had lower weight gains than the one with M = Hf but the opposite was the case at 1000 ^{o}C. The lowest parabolic rate constant was that of the alloy with M = Ti (k_p = 3.3 10^{-14} $g^2cm^{-4}s^{-1}$) at 800 ^{o}C and 1000 ^{o}C (k_p = 6.7 10^{-13} $g^2cm^{-4}s^{-1}$) and the alloy with M = Hf at 1200 ^{o}C (k_p = 5 10^{-12} $g^2cm^{-4}s^{-1}$). At 800 ^{o}C there was no spallation of the scales formed on all alloys. At 1000 ^{o}C only the scale formed on the alloy with M = Hf had spalled. At 1200 ^{o}C the scales formed on the alloys with M = Hf, Nb and M = Ti were partially and completely spalled, respectively. In the temperature ranges 800 – 1000 ^{o}C and 1000 – 1200 ^{o}C the alloys with M = Hf and M = Ti had the lowest activation energies for oxidation, the latter were obtained using Arrhenius plots

In all three cast alloys with Al/Si = 1 and M = Hf, Nb, Ti, the M_6Si_5, 5-3 silicides and Al_8Cr_5 aluminide s were formed. The Cr_3Si was also formed in the alloy with M = Hf, the Al_9Cr_4 aluminide in the alloys with M = Ti and Nb and the $Nb_{11}Si_8$ silicide in the alloy with M = Nb. The solubility of Si in Al_8Cr_5 and Al in Cr_5Si_3 respectively was highest with M = Nb, Ti and lowest with M = Ti, Hf. There was solubility of Al in M_6Si_5 for M = Hf, Ti which was essentially the same in the two alloy but the solubility was very low for M = Nb. The solubility of M in Al_8Cr_5 was very low for Hf, Ti, Nb. The lowest volume fractions were for Al_9Cr_4 in the alloys with M = Ti, Nb and the volume fraction of the Al_8Cr_5 aluminide was above 33% in all three alloys. The M_6Si_5 was stable in the heat treated microstructures of the alloys with M = Hf, Ti.

None of the alloys with Al/Si = 1 exhibited pest oxidation. The alloy with M = Nb had the highest weight gains at each oxidation temperature and the one with M = Hf had the lowest. At 800 ^{o}C the alloy with M = Hf had the lowest parabolic rate constant (k_p = 1.3 10^{-13} $g^2cm^{-4}s^{-1}$). At 1000 ^{o}C the alloys with M = Hf, Ti had the same rate constant (k_p = 3.3 10^{-12} $g^2cm^{-4}s^{-1}$) that was lower than that for M = Nb (k_p = 5.9 10^{-9} $g^2cm^{-4}s^{-1}$). At 1200 ^{o}C the alloy with M = Ti exhibited parabolic oxidation with k_p = 6.7 10^{-12} $g^2cm^{-4}s^{-1}$ compared with k_p = 1.6 10^{-8} $g^2cm^{-4}s^{-1}$ for M = Nb. The alloy with M = Hf exhibited cubic oxidation at 1200 ^{o}C. At 800 ^{o}C there was no scale spallation in all three alloys. At 1000 ^{o}C the scales were spalled, partially spalled and unspalled with M = Hf, Ti and Nb, respectively. At 1200 ^{o}C the corrugated scales formed on all three alloys were spalled along the ridges and the scale formed on the alloy with M = Hf was more protective than the scales formed with M = Ti and Nb.

At 800 ^{o}C all three alloys with Al/Si = 0.1 formed alumina, silica and mullite and with M=Hf, Nb, Ti, the oxides HfO_2, Nb_2O_5 and TiO_2, respectively. Chromia was also formed with M=Ti. For the alloys with Al/Si=1, continuous alumina scale with silica islands was formed with M=Hf, and alumina, silica and mullite with M=Nb, Ti and chromia with M=Ti. At 1000 ^{o}C, for Al/Si=0.1 the scale with M=Hf was silica, mullite and $(Al,Cr)_2O_3$ and silica, mullite, alumina and chromia with M=Nb, Ti. Hafnia and titania formed with M=Hf, Ti but not Nb_2O_5 with M=Nb. For

Al/Si=1 continuous alumina with dispersed mullite formed with M=Hf. Only alumina formed with M=Ti and alumina, chromia and Nb_2O_5 formed with M=Nb. At 1200 °C, alumina formed with M=Ti and $(Al,Cr)_2O_3$ with M=Hf, Nb and mullite with the latter addition. For Al/Si=1 $(Al,Cr)_2O_3$ and mullite formed with M=Hf, Nb, Ti. No HfO_2, Nb_2O_5 and TiO_2 were formed in the alloys with Al/Si = 0.1 and 1.

The results of this study indicate that the quaternary addition of Hf, Ti and Nb could form the alumina scale without having high concentration of Al in the alloy with Al/Si=0.1 and achieve oxidation rate constants that are comparable to those of Ni and Pt based intermetallic alloys. The alloys with higher Al/Si=1 with the quaternary addition of Hf and Ti and Nb could form the alumina scale with rather higher oxide growth rates compared with former alloys; however, the formation of low melting point Al-Cr aluminide(s) in the microstructure has detrimental effect on their oxidation behaviour.

Dedicated to:

“My parents, ***Ramezan*** *and* ***Mahin-naz***
My wife, ***Mastan*** *and my son,* ***Daniel****”*

Acknowledgements

Firstly, I would like to offer my deepest gratitude to my supervisor Prof. Panos Tsakiropoulos for his continuous support, encouragement, motivation, supervision and useful suggestions during this study.

The financial support by the Immpetus group and University of Sheffield is gratefully acknowledged.

I sincerely thank Dr. Peter Korgul, Dr. Cathy Shields and Mr. Tim Hopkins for showing and teaching me how to use effectively the SEM, EBSD, EDS and EPMA, Mr. Philip Staton for his technical support in the specimen preparation, Mr. Bater Stuart for his technical support in heat-treatment, Dr. Zifu Li, Dr. John Plumber for their help in using of arc melter, Dr. Nik Reeves-McLaren for his training in X-ray diffraction analysis, and Dr. Claire Utton, Ms. Bev Lane and Mr. Andrew Mould for DSC and TGA training.

Finally, I would like to thank my family: my parents who have always supported me in all my pursuits; my loving wife, Mastan, without whose love, patience, understanding and encouragement I would not have completed this work; and most of all, my little son, Daniel, who has brought great joy to my life. I love you all.

Design and development of Cr-Si based intermetallic alloys

Contents

List of Figures

List of Tables

Nomenclature

BB	Bragg Brentano geometry
Bcc	Body-centered cubic
BSE	Backscatter Electron
CALPHAD	CALculation of PHAse Diagrams
DSC	Differential Scanning Calorimetry
DTA	Differential Thermal Analysis
EBC	Environmental Barrier Coating
EBSD	Electron Backscatter Diffraction
EBSP	Electron Backscatter Pattern
EDX	Electron Dispersive X-ray spectroscopy
EPMA	Electron Probe Micro Analysis
Fcc	Face –centered cubic
FEG	Field Emission Gun
GXRD	Glancing Angle X-Ray Diffraction
Hcp	Hexagonal closed pack
ht	high temperature
HV	Vickers Hardness
JCPDS	Joint Committee of Powder Diffraction Standards
kV	kilo Volt
L	Liquid
mA	milliamp
MAD	Mean Angular Deviation
NIST	National Institute of Standards and Technology
rt	room temperature

SE	Secondary Electron
SEM	Scanning Electron Microscopy
TBC	Thermal Barrier Coating
TG	Thermo-Gravimetric
TGA	Thermo-Gravimetric Analysis
TGL	Thermally Grown Laves phase
TGO	Thermally Grown Oxide
WD	Working Distance
XRD	X-Ray Diffraction

1. Introduction

The search for new ultra-high temperature alloys to replace Ni based superalloys in future generation aero-engines has concentrated on refractory metal intermetallic based alloys, in particular Nb silicide based alloys and Mo silicide based alloys. For moving components such as blades, the former alloys are preferred owing to their low densities (~ 7 g/cm^3) compared with Ni based superalloys (~ 9 g/cm^3) and Mo silicide based alloys (> 9 g/cm^3).

The Nb silicide based alloys are based on Nb-18 at.% Si with simple metal and metalloid (Al, B, Ge, Sn), transition metal (Cr, Fe, Hf, Ti, Zr) and refractory metal (Mo, Ta, W) alloying additions. These alloying elements are used to enhance the properties of the bcc Nb solid solution and to stabilise desirable intermetallics, such as tetragonal Nb_5Si_3 and $NbCr_2$ Laves, to achieve a balance of room, intermediate and high temperature mechanical properties, and oxidation resistance. These alloys have the potential to enter service where surface temperatures will exceed 1350 ^{o}C. Improved oxidation behaviour that meets the oxidation goals of the industry for the uncoated alloy is required for the successful implementation of the Nb silicide based alloys. Thus, the alloys must have some inherent oxidation resistance and in service will be coated, like the superalloys [1].

The coating systems used on state of the art Ni based superalloys in the hottest parts of the gas turbine are of the TBC (thermal barrier coating) type. The typical structure of the TBCs consists of a top coat, an (in situ) thermally grown oxide (TGO) and a bond coat, as shown in Figure 1.1. The top coat is a ceramic coat (typically YSZ = yttria stabilised zirconia), the bond coat is a thin layer of an intermetallic based alloy such MCrAlY (M=Ni, Co) or PtAl aluminide and the TGO is α-Al_2O_3. The bond coat plays an important role in the durability of TBCs. The TBCs used in gas turbines offer a balance of properties regarding thermal and mechanical stresses, interaction between components and response to erosive and corrosive environments [2, 3]. For further improvements, Takahashi et al. [4] proposed multilayer system consisting of five layers on a superalloy substrate with each layer having its own unique functions.

For long-term ($\gg$ 1000 h) use above about 600 ^{o}C, the oxides Al_2O_3, Cr_2O_3 and SiO_2 are desirable. These oxides offer the potential for protection if they are formed as continuous layer because the rates of metal and oxygen diffusion in them are sufficiently low so that they grow at an acceptably slow rate [5]. For long-term service under isothermal conditions, Cr_2O_3 scales can provide protection up to a maximum temperature of about 1000-1100 ^{o}C; Al_2O_3 to around 1400 ^{o}C; and SiO_2 to about 1700 ^{o}C. There is also a volatility disadvantage for both Cr_2O_3 and SiO_2 scales during high temperature oxidation in the presence of water vapour, which can significantly reduce their maximum-use temperature. In general, the volatility of oxide species is dependent on oxygen pressure, H_2/H_2O pressure and the vapour pressure of species. By increasing the water vapour pressure, the oxygen pressure decreases and consequently lower oxide species with higher vapour pressure such as SiO evaporate. For chromia in the presence of water vapour pressure, the Cr(g) species has highest vapour pressure for $p(H_2/H_2O) > 0.3$ atm and evaporates upon oxidation. Brady and Tortorelli [6] have produced a comprehensive review to classify the aspects of alloy design that must be considered for protective scale formation on intermetallics. These include thermodynamic stability, oxygen solubility, multi-phase phenomena, and subsurface depletion.

Research on potential coatings for Nb silicide based alloys has pointed to coating systems that will have multi-component architectures consisting of metallic and ceramic materials. The coating system should be capable of forming in-situ alumina (preferred) or silica and possibly chromia, or mixtures of these oxides.

Intermetallic-based alloys will be used in these systems; as such, materials are capable of exhibiting good oxidation at high temperatures. Knowledge of how intermetallic-based alloy composition and microstructure can be manipulated to influence their oxidation at $T > 1100$ ^{o}C is key factor to designing and developing multi-component high temperature coatings. It is also very important to consider on what constituent of a protective scale depends the desired lifetime of components under the expected service conditions.

The concept of a multi-component coating system for Nb silicide based alloys can be best demonstrated using the coating system that has been proposed by Jackson, Bewlay et al [7,8]. It contains multiple layers, as is shown in Figure 1.2 that act as diffusion barrier, bond coat, and topcoat. Depending on coating system, the intermetallic phases may be a silicon modified C14-Cr_2Nb Laves phase and optionally a chromium solid solution phase, a CrNbSi intermetallic phase, and/or an M3Si intermetallic phase or M_5Si_3, MSi_2 and/or M_3Si_2 where M=Mo, Nb, Ti, Cr, Hf, Fe, Ta and/or W [8]. The diffusion barrier itself comprises three layer, bond coat, thermally grown oxide (TGO) and thermally grown Laves phase (TGL). The Laves phase layer contains the C14 (hexagonal) (Nb,Ti)$(Cr,Si,Al)_2$ Laves.

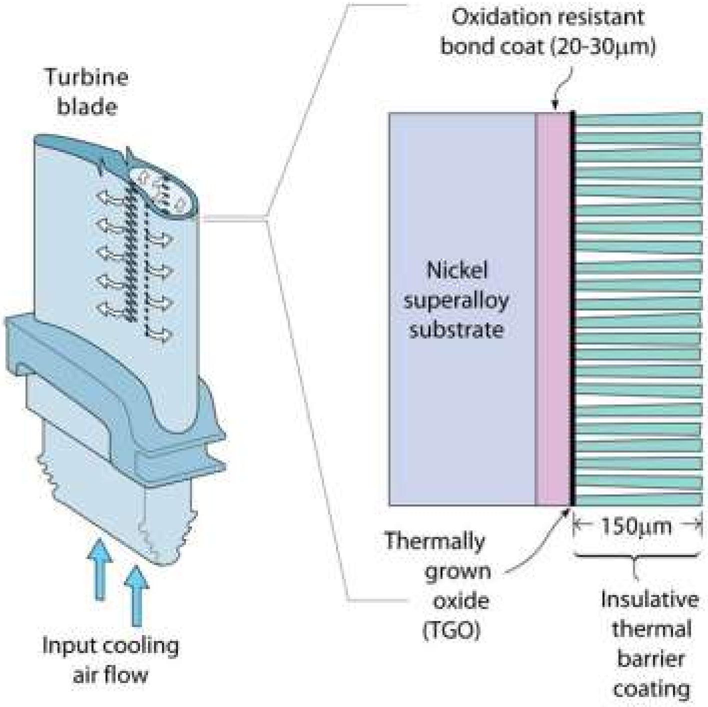

Figure 1.1 Schematic of TBC used for the Ni superalloy [9].

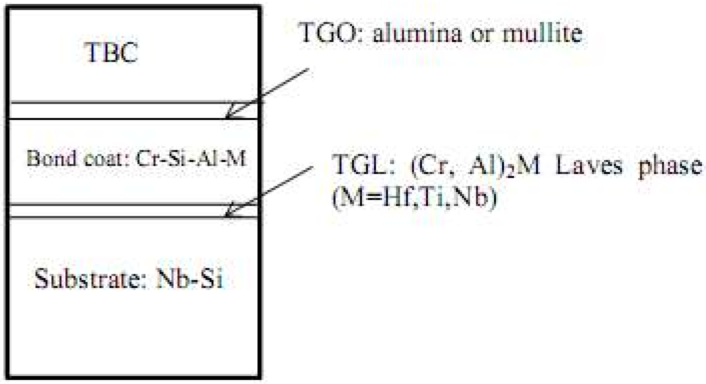

Figure 1.2 Schematic of TBC for Nb-Si [8]

The objective of the present study is to design and develop oxidation resistant alumina and silica (and possibly chromia)-forming intermetallic alloys. Such alloys could become components of a multi-material bond coat of a coating system of the Thermal Barrier Coating (TBC) type applied to Nb silicide based alloy substrates. Producing coatings on selected Nb silicide based substrate(s) is not an objective of this project (in other words coated substrate(s) are not studied in this thesis).

Considering the types of desirable oxides and the chemistry of Nb silicide based alloys discussed above, this research will concentrate on Cr-Si-Al alloys with a quaternary addition of a transition or refractory metal. To our knowledge, study of such Cr-Si-Al-X quaternary alloys as potential bond coat type alloys has not been reported. As a starting point, the Cr-Si-Al base alloys will be chosen with two Al/Si ratios, and the quaternary additions will each be added at 5 at%. The quaternary additions will be selected from the typical alloying elements of Nb silicide based alloys (see above).

Considering an Nb silicide based alloy/Cr-Si-Al system, diffusion of species across the interface would be expected. If there were to be upward diffusion of Nb, Ti and Hf and downward diffusion of Cr and Al (and possibly Si) $NbCr_2$ Laves formation at the interface could be possible (Al and Si stabilize the C14-$NbCr_2$ and Hf and Ti form Laves phases). The unalloyed $NbCr_2$ Laves is stable to ~ 1668 ^{o}C, has very good oxidation, but suffers from poor toughness. However, if too much Al were to diffuse to the substrate its DBTT would increase about -50 ^{o}C, which is undesirable, and if too much Cr were to diffuse to the substrate then its liquidus temperature would be reduced, which is also undesirable. Therefore, Laves phase formation at the interface requires careful choice of Al and Si concentrations in the Cr-Si-Al coating. The above point to considering the choice of Hf, Nb and Ti as quaternary additions.

The structure of the thesis is follows. A brief review of relevant literature with emphasis on phase equilibria for binary and ternary systems of interest is presented in chapter 2. The oxidation of alumina forming and silica forming alloys is briefly reviewed in chapter 3. The selection of alloys, their production, and techniques used for the characterisation of their microstructures and assessment of their oxidation are presented in chapter 4. Chapter 5 to 7 present and discuss the results for alloys with the aforementioned quaternary additions. The conclusions of this research and suggestions for future work are given in chapter 8.

2. Phase equilibria in binary and ternary systems

2.1 Background

Intermetallic compounds are currently being considered for a variety of high temperature applications because they can potentially offer a combination of creep resistance and low density, which are superior to those provided by state of the art coated and internally cooled Ni-based superalloys. The achievement of adequate oxidation resistance in these materials, which possess high specific strengths, is a matter of concern. Selective oxidation and the transition to internal oxidation have been investigated on various alloy systems and this knowledge can be implemented when designing coatings for high temperature applications. The effects of temperature on the transition to external oxidation and on the occurrence of pest oxidation have been a very important subject of research together with kinetics of oxidation and possible mechanisms since the 1970s.

Cr-Si-Al alloys show good oxidation resistance with no mass loss after oxidation in air at elevated temperature (>1000 ^{o}C) [10]. They might be used as coating materials for carbon/carbon composites as well as metallic substrates. Similar to the conventional Ni superalloys, the carbon/carbon composites will need a coating system to protect them from oxidation at service temperature. In addition, they also need an additional coating system to be protected from degradation by water vapour. The development of oxidation resistance in alloys is based on the addition of element(s) that will oxidize selectively and produce a protective oxide scale. The formation of the scale layer requires the oxide to be more stable than the lowest oxide of the base metal. The microstructure of the alloys is important for controlling the kinetics of oxidation. As already mentioned in the introduction, the protective oxides are alumina, silica and chromia, and these are used to protect the substrate from oxidation. The oxides Al_2O_3, SiO_2 are of principal interest because they exhibit low diffusivities for cations and anions as well as being highly stable above 1000 °C. An α-Al_2O_3 scale offers best protection for metallic materials against high temperature corrosion in oxidizing environments due to the very low defect concentration and good compactness.

Chromium oxide offers advanced technological applications owing to high hardness, resistance to oxidation (<1050 ^{o}C), and high refractoriness. It also exhibits low friction coefficient and high resistance to wear and corrosion. These properties allow it to be used as a protective coating in tribological applications. Mechanical and adhesion properties of coatings are affected by microstructure. Different stoichiometric ratios exhibit vastly different mechanical properties in chromium oxide coatings. High adhesion is known to ensure the prolonged lifetime of the coating and to promote good wear resistance. Good coating adhesion is required for wear- and corrosion resistance applications. Premature failures can occur for many reasons, including coating delamination, cracking, and plastic deformation [5].

The best Ni and Co based alloys are inadequate for sustained application at temperature above 1050 °C under constant load and further development of these alloys is limited, as future turbine entry temperatures will be above the melting point of the base metal. The refractory metals Mo and Nb have adequate strength up to about 1300 °C but poor oxidation resistance [6]. Coatings for alloys based on Nb and Mo with improved oxidation resistance are being studied, as like the Ni based superalloys, the refractory metal alloys will require oxidation resistant coatings.

Chromium based alloys have been considered for high temperature applications, owing to the high melting point, low density, high thermal conductivity and fairly good oxidation resistance of Cr [11]. The brittleness of Cr however is a weakness, which can be rectified in different ways. One potential solution to the brittleness problem is to form an in situ composite composed of a ductile matrix phase to provide toughness, reinforced by a Cr_2X (X= Ti, Hf, Nb) Laves phase for high temperature strength.

For high temperature alloy development two general approaches to Laves phase containing in-situ composites have been exploited: a Nb(Cr) solid solution based matrix and a Cr(X) (X= Al,Si,Ti,Ta) solid solution based matrix [12]. Two key properties from an alloy development standpoint are intermediate and high temperature oxidation and room temperature fracture toughness. An intermetallic-based alloy to be used as coating material to increase oxidation resistance should be compatible with the substrate. To design and develop new alloys with optimized key properties, reliable data on phase equilibria is necessary. Knowledge of phase equilibria is required to optimize the composition of coating alloy(s) to provide protection via alumina, silica and chromia scales. This literature survey aims to review Cr based binary Cr-X [X=Al,Si,Ti,Hf,Nb], M-Al and M-Si binary (M=Hf,Ti,Nb) and ternary Cr-Si-X [X=Al, Ti, Hf] alloy systems to understand phase equilibria in developmental alloys. The survey also addresses briefly the oxidation behaviour of alloys forming alumina, silica, and chromia.

2.2 The Cr-Si binary system

The phase diagram of the binary Cr-Si system has been investigated by many researchers using differential thermal analysis (DTA) up to 1500 °C [13]. Figure 2.1 shows the Cr-Si phase diagram [14] as updated by Du et al. [15] based on thermal analysis measurements of the CrSi-Si partial system and thermodynamic modeling of the entire system.

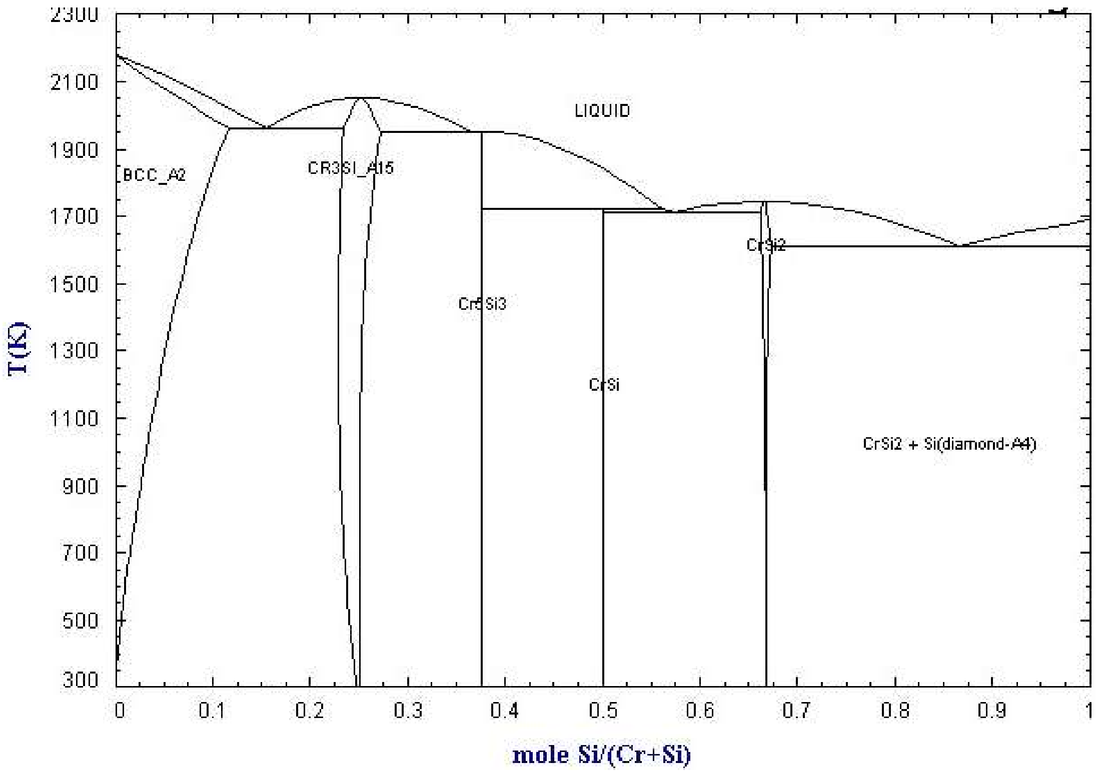

Figure 2.1 The phase diagram of the Cr-Si system [14]

In the Cr-Si binary system, there are four intermetallics with melting points in the range 1400 to 1780 °C. The Cr_3Si, Cr_5Si_3 and $CrSi_2$ melt congruently at 1780, 1666 and 1439 °C respectively, and the CrSi melts incongruently at 1424 °C. The tetragonal Cr_5Si_3 is of the W_5Si_3 type and thus isomorphous with β Nb_5Si_3 and Mo_5Si_3.

2.3 The Cr-Al binary system

Liang et al. [16] studied the Cr-Al system. The phase equilibria is shown in Figure 2.2. In the binary, there are a number of intermetallic phases, namely $CrAl_7$, Cr_2Al_{11}, $CrAl_4$, Cr_4Al_9, Cr_5Al_8 and Cr_2Al. Aluminum has a large solubility in Cr, 46 at. % at 1350 °C. The Cr_5Al_8 is stable up to about 1316 °C. Cr_5Al_8 is the first phase to form from the melt in the composition range 38 to 41.5 of Cr (at. %).

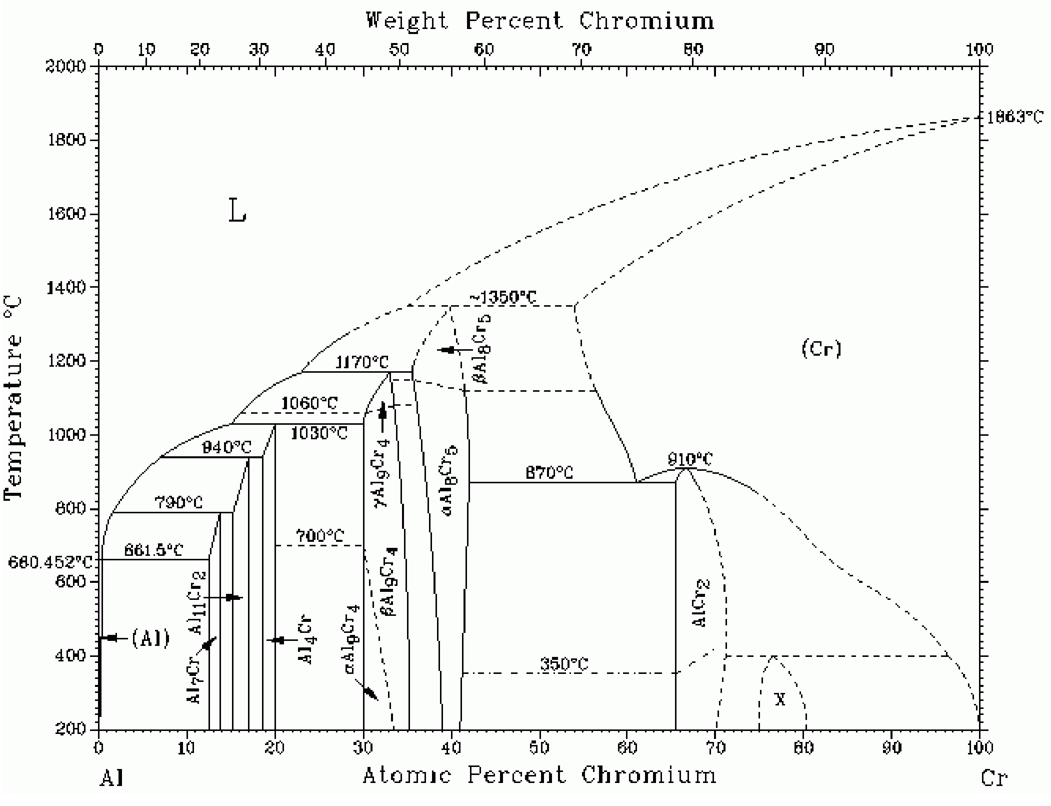

Figure 2.2 The phase diagram of the Cr-Al system [17]

2.4 The Cr-Hf binary system

There are six phases in the Cr–Hf binary system, namely liquid, bcc (Cr), bcc (Hf), hcp (Hf), $HfCr_2$ (C14), and $HfCr_2$ (C15), see Figure 2.3. Carlson and Alexander (referenced in [18]) and

Svenchnikov et al (referenced in [18]) studied the phase equilibria of the Cr–Hf system. In 1975, Kaufman and Nesor [19], using existing experimental results, carried out the first thermodynamic modeling for this system. However, the thermodynamic description developed by Kaufman and Nesor used the lattice stability data for pure elements Cr and Hf that were different from those used for the Cr–Si and Hf–Si binaries, and the currently accepted SGTE (Scientific Group Thermodata Europe) data. Venkatraman and Neumann [20] carried out a critical review on all experimental data up to 1986 for the Cr–Hf system. Based on the assessment of Venkatraman and Neumann, a thermodynamic model was built for the Cr–Hf system in [18] and the calculated binary is shown in Figure 2.3.

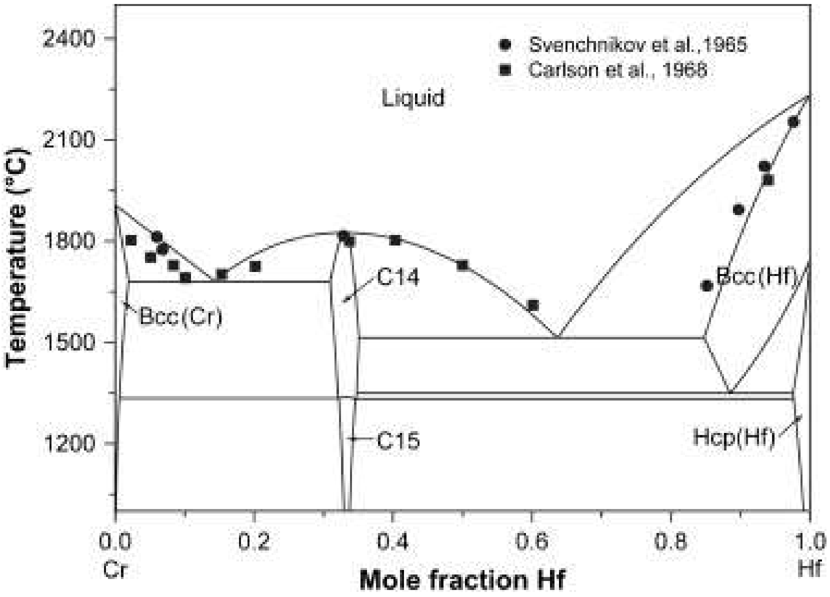

Figure 2.3 The phase diagram of the Cr-Hf system [18]

2.5 The Cr-Ti binary system

The Cr-Ti phase diagram is shown in Figure 2.4 and contains six phases:

1. The liquid phase
2. The solid solution α phase with 2 at% solubility of Cr in Ti at about 650 ^{o}C
3. The solid solution β phase, in the whole range of chromium solubility in titanium
4. The α -TiCr_2 Laves phase with the C15 crystal structure (shown as the TiCr_2 rt phase in Figure 2.4)

5. The β -$TiCr_2$ phase with the C36 crystal structure (shown as the $TiCr_2$ ht1 phase in Figure 2.4)
6. The γ -$TiCr_2$ phase with the C14 crystal structure (shown as the $TiCr_2$ ht2 phase in Figure 2.4)

The Cr-Ti system shows a minimum liquid temperature of 1410 ^{o}C at ~ 60 at. % Ti. The Laves phases are cubic $TiCr_2$ (α) with $MgCu_2$ type structure (C15) and hexagonal $TiCr_2$ (γ, β, [5, 21]). The latter phase exists in two allotropic forms $TiCr_2$ (high temperature, low temperature), which possess the $MgZn_2$ and $MgNi_2$ – type structure (C14, C36), respectively which differ only in atomic layering [22]. There is no solubility of Ti in Cr at room temperature.

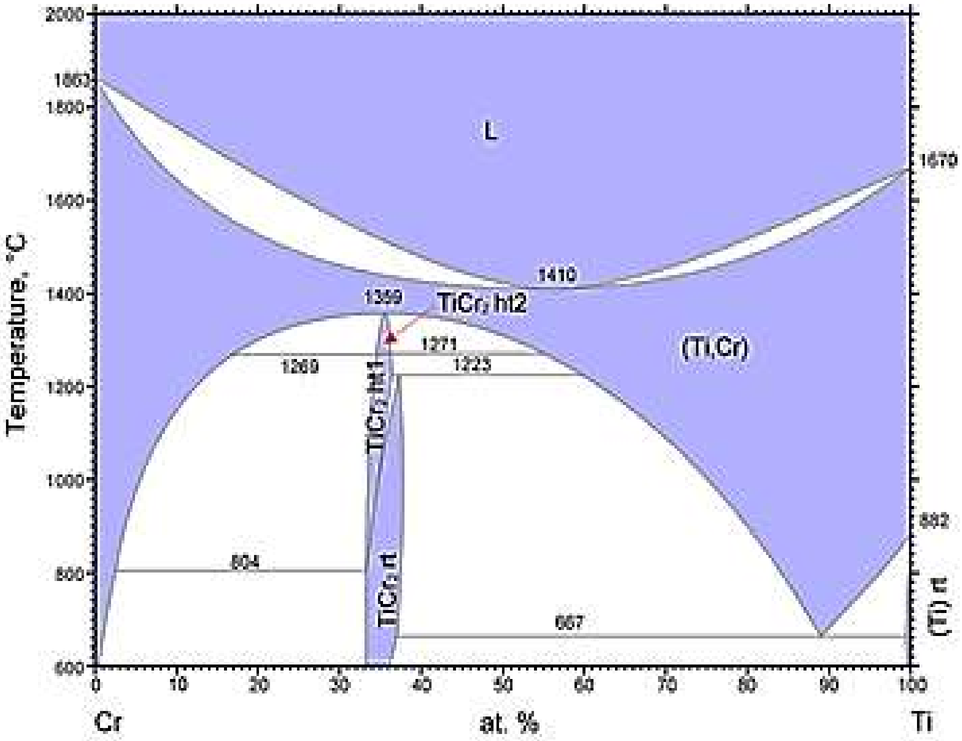

Figure 2.4 The phase diagram of the Cr-Ti system [23]

2.6 The Cr-Nb binary system

The phase diagram of the binary Cr-Nb system is shown in Figure 2.5. There are five equilibrium phases in the system, namely, the liquid (L), the high temperature Laves phase with hexagonal lattice [C14-$NbCr_2$], the low temperature Laves phase with cubic lattice [C15-$NbCr_2$], and the body -centered cubic (bcc) solid solutions Nb_{ss} and Cr_{ss} . There are also two eutectic reactions between the Laves phase $NbCr_2$ and the two solid solutions. The Nb –rich eutectic reaction between the $NbCr_2$ and Nb_{ss} occurs at ~ 12 at. % Nb and 1620 ^{o}C, and the Cr-rich eutectic between the $NbCr_2$ and Cr_{ss} at ~ 50 at. % Nb and 1650 ^{o}C. The C14-$NbCr_2$ is stable between 1585 and 1770 ^{o}C, and transforms to the C15-$NbCr_2$ between 1585 ^{o}C and 1625 ^{o}C depending on the alloy composition. The Cr maximum solid solubility in Nb_{ss} is ~ 15 at. % at 1650 ^{o}C.

A modification of the Cr-Nb binary system has been proposed by Thoma and Perpezko [24], as shown in Figure 2.6, for the eutectic composition and temperature, the solubility of constituent phases and phase boundaries. There is good agreement between the modified Nb-Cr binary system and the one proposed by Venkatraman and Neumann [25].

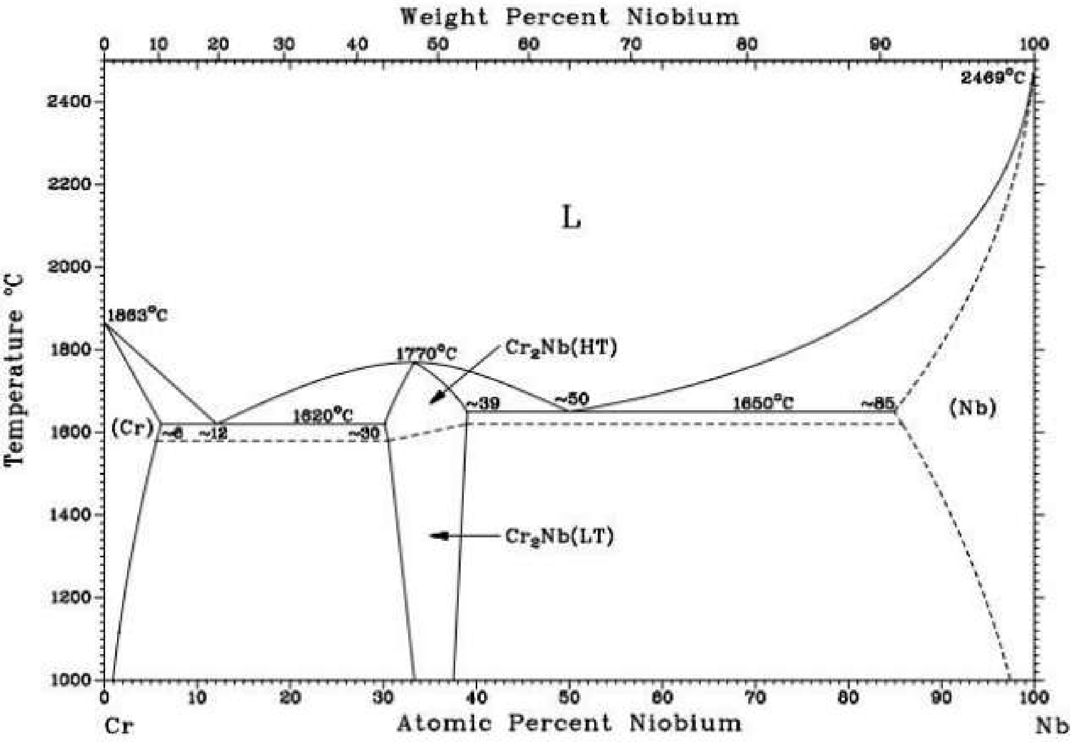

Figure 2.5 The Cr-Nb phase diagram [25]

Therefore, the data for the Cr-Ti, Cr-Hf, Cr-Ta and Cr-Nb binaries shows that Ti, Hf, Ta and Nb can form with Cr hexagonal C14 and cubic C15 Laves phases, of which the high temperature phase has the C14 structure ($MgZn_2$-type).

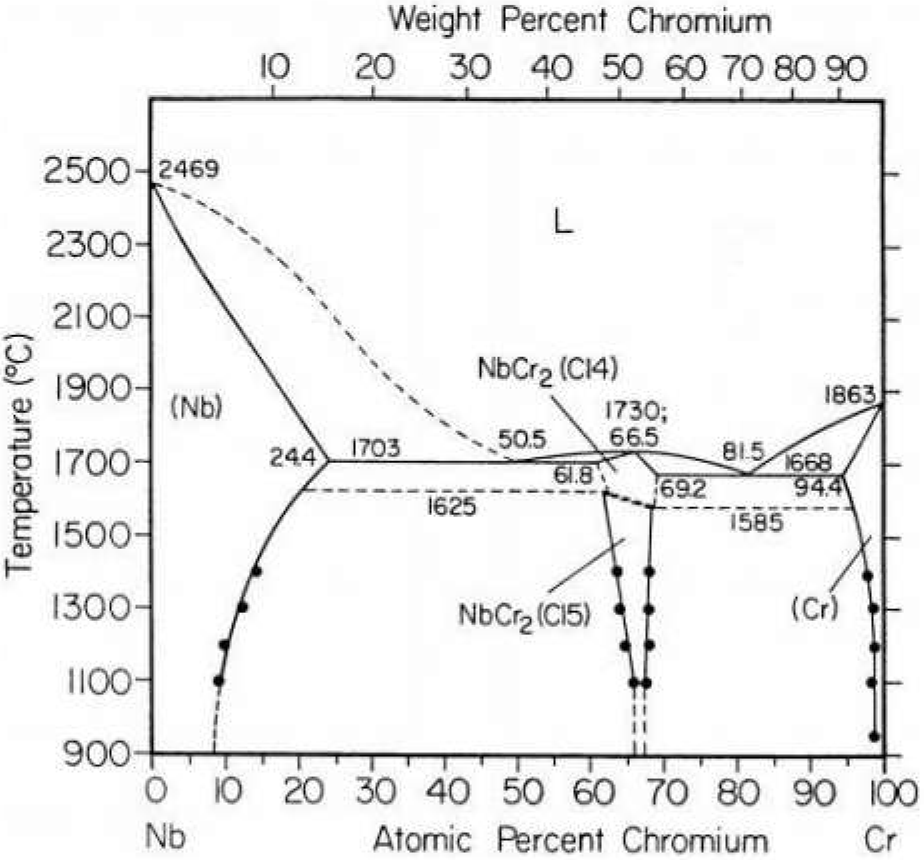

Figure 2.6 The revised Cr-Nb phase diagram [24].

2.7 The Hf-Al binary system

Tsyganova et al. [26] and Murray et al. [27] reviewed the phase equilibria in the Hf-Al system. Kaufman and Nesor [19] also performed the calculation of the Hf-Al binary system in 1975. Wang et al [28] recently performed thermodynamic assessment of the Hf-Al binary system. The assessed phase diagram (Figure 2.7) includes: (1) the liquid phase, (2) three terminal solid solutions (bbc Hf, cph Hf, and fcc Al) and (3) seven intermediate compounds, Hf_2Al, Hf_3Al_2, Hf_4Al_3, HfAl, Hf_2Al_3, $HfAl_2$, and $HfAl_3$. Amongst these intermetallic compounds the Hf_3Al_2, HfAl, $HfAl_2$ and $HfAl_3$ melt congruently respectively at 1590, 1800, 1650 and 1590 °C whereas the Hf_2Al, Hf_4Al_3 and Hf_2Al_3 melt incongruently respectively at 1200, 1400 and 1640 °C. The HfAl has the highest melting point amongst all intermetallic compounds in the Hf-Al system (Tm= 1800 °C). The maximum solubility of Al in Hf is 27 and 33 at.% for the α-Hf and β-Hf solid solution respectively at 1450 and 1530 °C. The homogeneity ranges are quite narrow for all intermediate phases. Thus, they can be treated as stoichiometric compounds. There are two polymorphs for the $HfAl_3$ that can transform to one another at 650 °C. The solubility of Hf in fcc Al is negligible up to 700 °C and it increases to about 10 at.% at about 1400 °C.

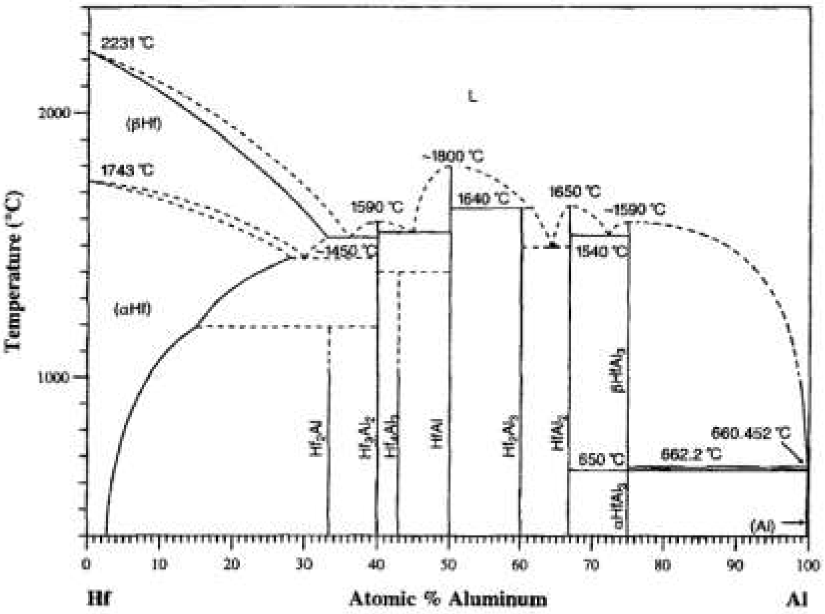

Figure 2.7 The Hf-Al phase diagram [27].

2.8 The Hf-Si binary system

Gokhale and Abbaschian [29] assessed the Hf-Si phase diagram using the experimental results of Brukl. Zhao et al. [30] proposed a new version of the Hf-Si binary phase diagram. The Hf-Si system (Figure 2.8) contains nine stable phases: the liquid phase (L), the α Hf and β Hf solid solutions, the tetragonal Al_2Cu-type Hf_2Si, the tetragonal Si_2U_3-type Hf_3Si_2, the hexagonal Mn_5Si_3-type Hf_5Si_3, the tetragonal Zr_5Si_4-type Hf_5Si_4, the orthorhombic BFe-type HfSi, the orthorhombic $ZrSi_2$-type $HfSi_2$ and the diamond cubic type solid solution Si.. In the revised phase diagram, the existence of the Hf_5Si_3 intermetallic was confirmed as well as the reactions:

$Hf_3Si_2 + L \rightarrow Hf_5Si_3$ at 2357 °C

$Hf_5Si_3 \rightarrow Hf_3Si_2 + Hf_2Si$ at 1924 °C

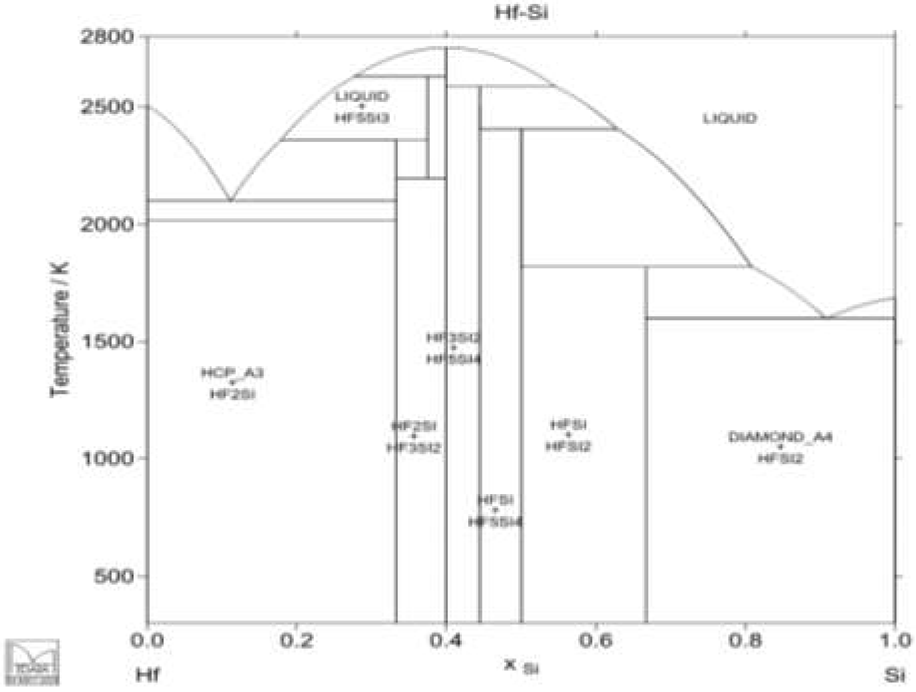

Figure 2.8 The phase diagram of the Hf-Si system [30]

The crystal structures of phases in the Hf-Si binary are given in Table 2-3 below in the section about the Cr-Hf-Si ternary.

2.9 The Ti-Al binary system

There are many versions of the Ti-Al binary phase diagram. A controversial area of the phase diagram is between 55 and 77 at. % Al, and 900 to 1450 ^{o}C. In Figure 2.9 [31] the dashed lines indicate estimated transformation curves. There are four intermetallic compounds with solubility range ($AlTi_3$, AlTi, Al_2Ti, δ), and one line compound (Al_3Ti). At T ≈ 1285 ^{o}C and $X_{Al} \approx 45$ at. % a peritectoid transformation occurs. The liquidus and solidus curves of $L \leftrightarrow \beta_n$ show a maximum that in other works does not occur. The transformations of the intermetallic compounds are:

- Peritectic transformations:

$$L_{0,53} + \left(\beta_{Ti}\right)_{0.51} \xleftrightarrow{1480\,°C} \left(AlTi\right)_{0.475}$$

$$L_{0.735} + \left(AlTi\right)_{0.695} \xleftrightarrow{1380\,C} \delta_{0.715}$$

$$L_{0.8} + \delta_{0.725} \xleftrightarrow{1350\,°C} \left(Al_3Ti\right)_{0.75}$$

- Peritectoid transformation:

$$\left(AlTi\right)_{0.65} + \delta_{0.725} \xleftrightarrow{1240\,°C} \left(Al_2Ti\right)_{0.67}$$

- Order-disorder transformation:

$$\left(\alpha_{Ti}\right)_{0.309} \xleftrightarrow{1180\,°C} \left(AlTi_3\right)_{0.309}$$

A modified Ti-Al diagram by Okamoto [32] is shown in Figure 2.10. There are three intermetallic compounds with solubility range ($AlTi_3$, AlTi, and Al_3Ti) and two line compounds (Al_2Ti, Al_5Ti_2). Some experimental data differs from others, for example the peritectic transformations of Al_3Ti (1387 °C, versus 1392.5 °C in [32]) and AlTi (1460 °C, versus 1462.6 °C in [32]). The crystal structures of intermetallic compounds are listed in Table 2-1 [33].

Table 2-1 Crystal prototype of the intermetallic compounds in the Ti-Al binary system [33]

Intermetallic compound	prototype
Al_3Ti_{17}	Mg
Al_6Ti_{19}	Mg
$AlTi_3$	Ni_3Sn
$AlTi_2$	Ni_3Sn
Al_2Ti_3	Mg
AlTi	AuCu
Al_5Ti_3	-
Al_2Ti	Ga_2Hf
$Al_{11}Ti_5$	Al_3Zr
Al_5Ti_2	Al_5Ti_2
$Al_{23}Ti_9$	Al_3Ti
Al_3Ti	Al_3Ti

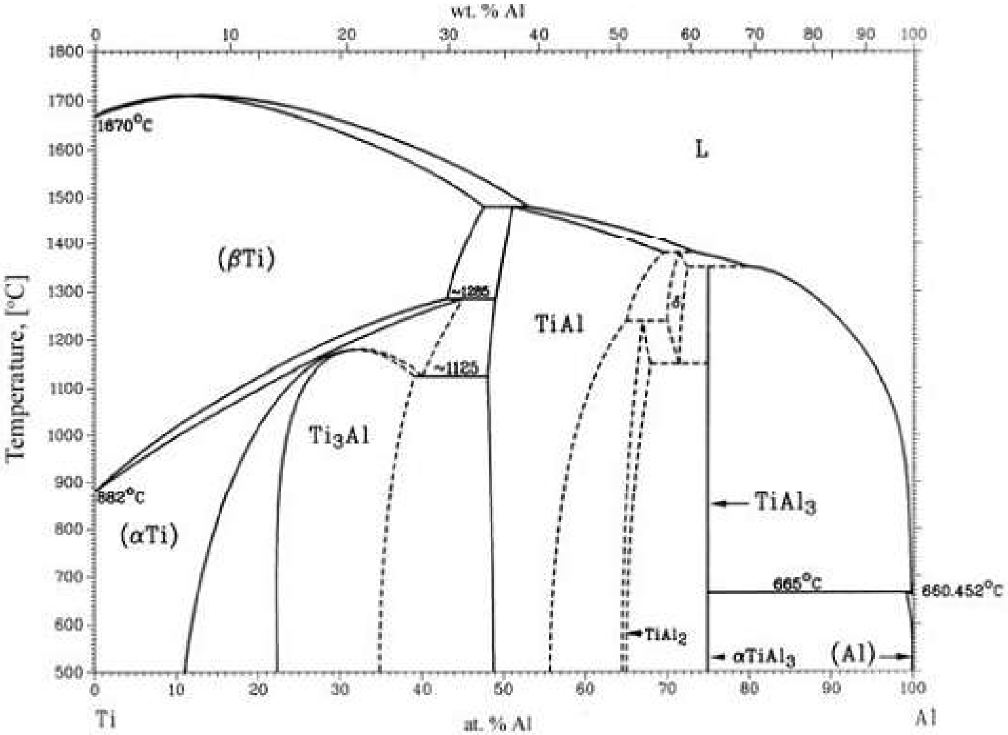

Figure 2.9 The Ti-Al phase diagram [31]

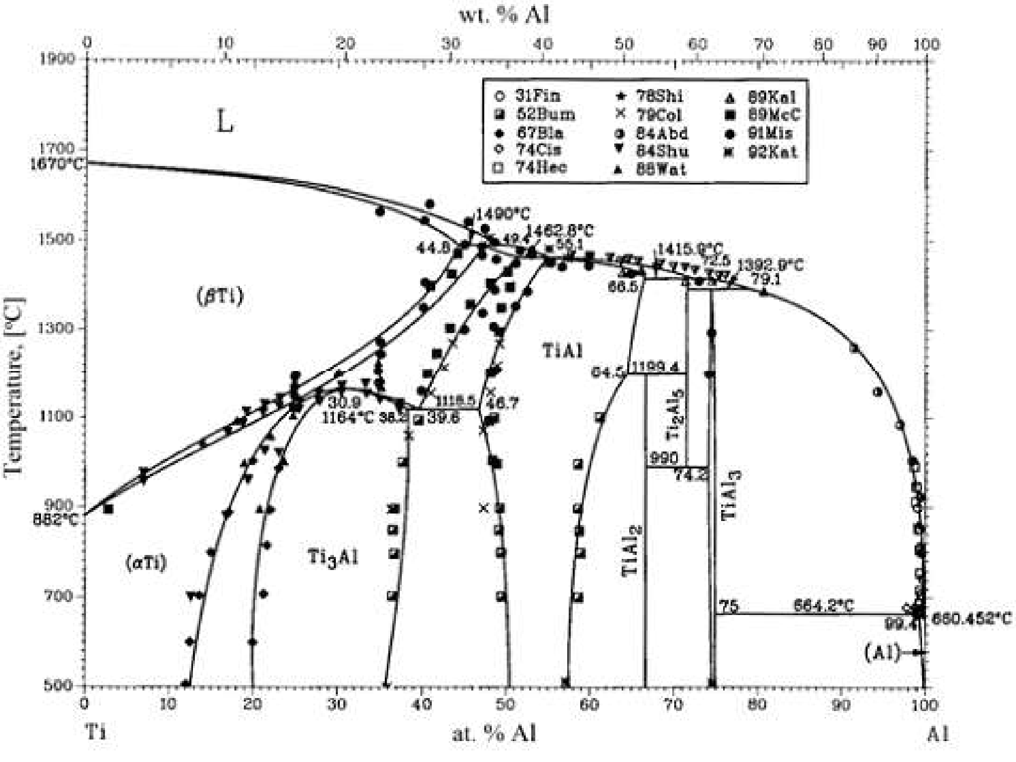

Figure 2.10 A modified Ti-Al phase diagram [32]

2.10 The Ti-Si binary system

The Ti-Si phase diagram (Figure 2.11) contains nine stable phases: the liquid (L), the bcc terminal solid solution (β Ti), and the hcp terminal solid solution (α Ti), the tetragonal Ti_3P-type Ti_3Si, the hexagonal Mn_5Si_3-type Ti_5Si_3 with a homogeneity range of about 4 at. %, the tetragonal Zr_5Si_4-type Ti_5Si_4, the stoichiometric TiSi, the stoichiometric $TiSi_2$ and the diamond cubic (Si) solid solution. The Ti_3Si and Nb_3Si phases are isomorphous, while the Ti_5Si_3 and Nb_5Si_3 are not isomorphous and have the tI32 and hP16 crystal structures, respectively [34]. The Ti_5Si_3 can form via a eutectic reaction at 1340 ^{o}C or congruently at 2122 ^{o}C, while the Ti_3Si phase forms by a peritectoid reaction between Ti_5Si_3 and (β Ti) at 1167 ^{o}C [31, 35, 36].

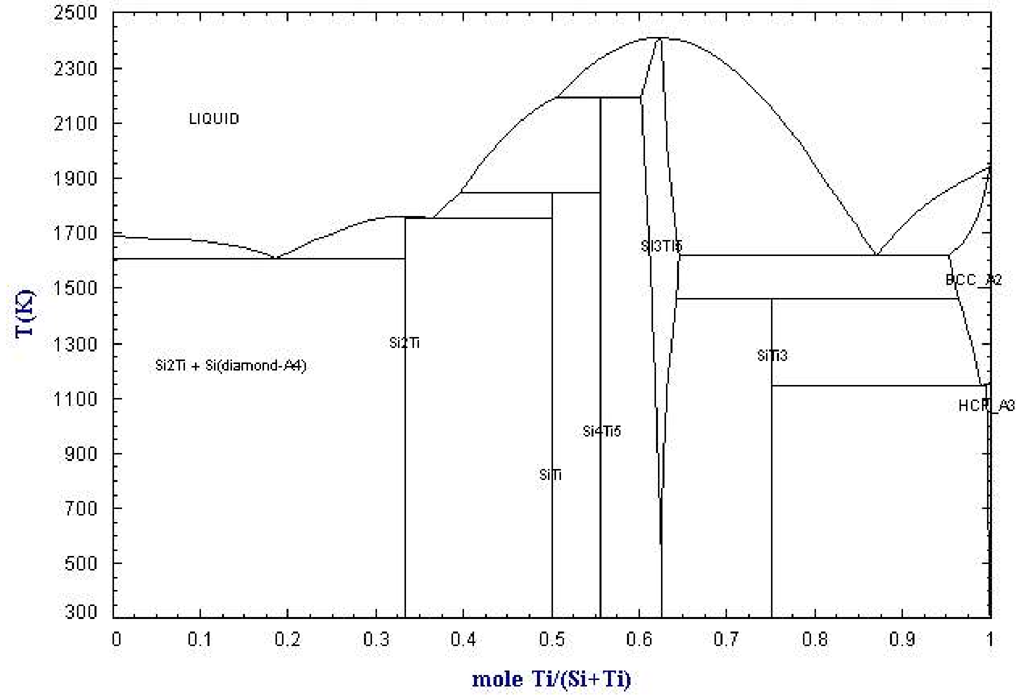

Figure 2.11 The Ti-Si phase diagram [36]

2.11 The Nb-Al binary system

The Nb-Al binary system is shown in Figure 2.12 [37]. The existence of the three intermediate compounds and the solid-solid phase boundaries of (Nb), Nb_3Al, and Nb_2Al are well established. The Nb-Al system is a relatively simple system with six phases: the liquid, L; the bcc (Nb) solid solution, which dissolves up to ~21.5 at.% Al at 2060 °C; Nb_3Al, with a maximum homogeneity range from 18.6 at.% Al below 1500 °C to 25 at.% Al at 1940 °C; Nb_2Al, with a maximum homogeneity range from 30 at.% Al below 1500 °C to 42 at.% Al at 1590 °C; $NbAl_3$, with a narrow homogeneity range with a width of ~1 at.%; and the fcc (Al) solid solution with extremely limited solubility of Nb. The Nb_3Al, and Nb_2Al melt incongruently and the $NbAl_3$ melts congruently. The A15 Nb_3Al intermetallic is formed by a peritectic reaction bcc + liquid $\rightarrow$ Nb_3Al (A15) at 2060°C. The phase limit of the Nb_3Al phase strongly depends on temperature. The Al-rich limit of the Nb_3Al phase includes the stoichiometric composition at the second peritectic temperature (1940°C). However, the Al-rich phase limit is shifted to lower Al concentrations with decreasing temperature, down to 21.5 at.% at 1000°C. The Nb_2Al intermetallic is also formed by a peritectic reaction Nb_3Al + liquid $\rightarrow$ Nb_2Al at 1940 °C.

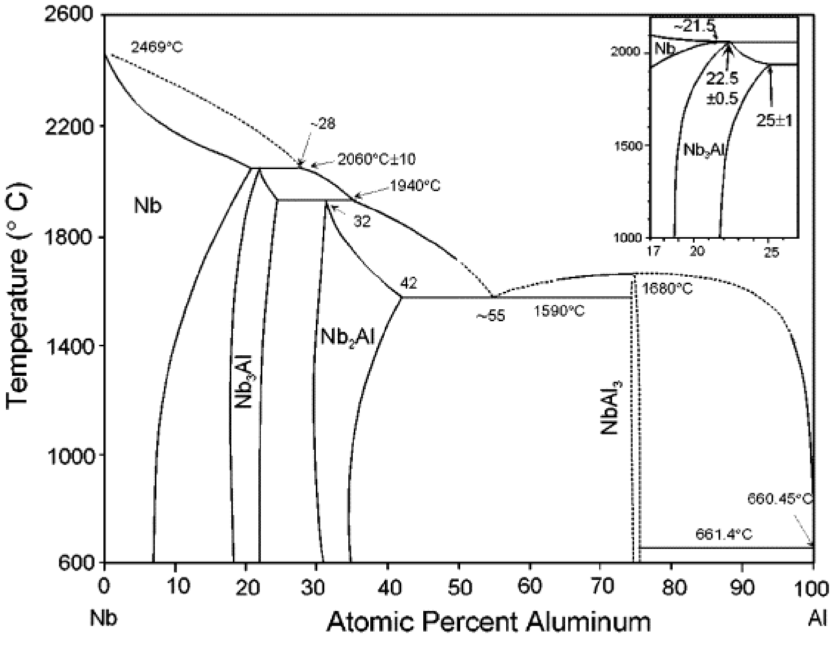

Figure 2.12 The Nb-Al phase diagram [37]

2.12 The Nb-Si binary system

The Nb-Si binary system in Figure 2.13 [38] contains seven phases: the liquid (L), the W-type Nb solid solution (Nb_{ss}), the tetragonal Ti_3P type Nb_3Si, the tetragonal W_5Si_3-type βNb_5Si_3, the tetragonal Cr_5Si_3-type αNb_5Si_3, the hexagonal $CrSi_2$-type $NbSi_2$ and diamond cubic type Si solid solution (Si_{ss}). The maximum solubility of silicon in the Nb_{ss} is 3.5 at.% at 1915 ^oC where the eutectic reaction is established. The βNb_5Si_3 and $NbSi_2$ both melt congruently at 2515 ^oC and 1935 ^oC respectively whereas metastable Nb_3Si melts incongruently at 1975 ^oC. The tetragonal βNb_5Si_3 and αNb_5Si_3 both have tetragonal crystal structures with a different lattice parameters and their homogeneity ranges are very narrow, about 4 at.% and 2 at.% Si respectively. The tetragonal Nb_3Si can be formed either a eutectic reaction or a peritectic reaction as follows:

$L \rightarrow Nb_{ss} + Nb_3Si$ eutectic reaction (at 1915 ^oC)

$L + \beta Nb_5Si_3 \rightarrow Nb_3Si$ peritectic reaction (at 1975 ^oC)

There is also a eutectoid reaction in the Nb-Si binary system that could stabilise simultaneously the Nb_{ss} and αNb_5Si_3 at 1765 ^oC.

$Nb_3Si \rightarrow Nb_{ss} + \alpha Nb_5Si_3$ eutectoid reaction (at 1765^oC)

Zhao et al [39] have proposed new eutectic and eutectoid temperature reaction temperature based on experimental results of directionally solidified Nb-Si alloys. They revised the eutectoid temperature to 1700 ^oC, and the eutectic temperature to 1880 ^oC at 18.2 at.% Si.

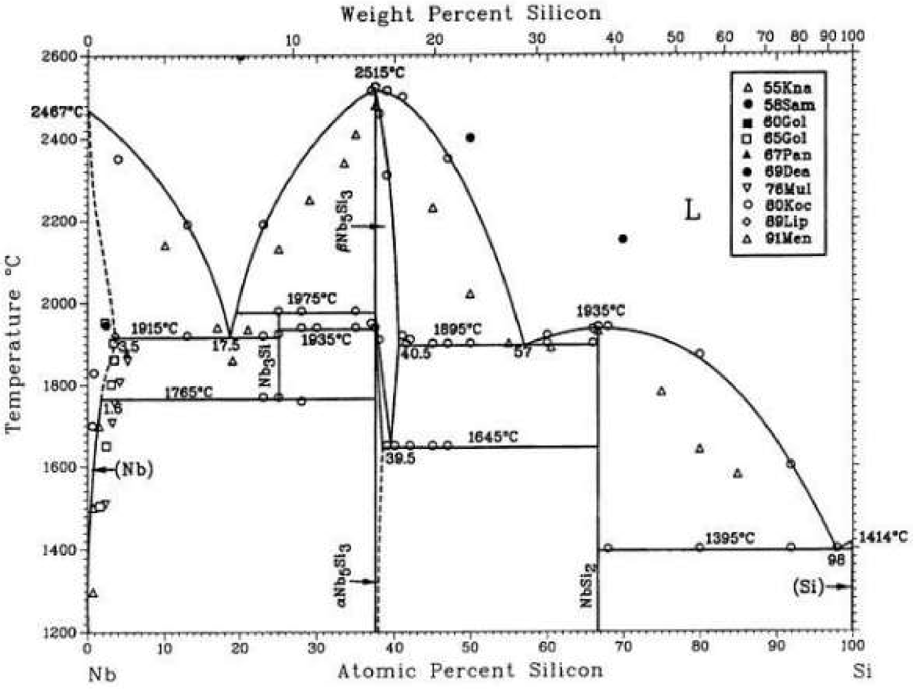

Figure 2.13 The Nb-Si phase diagram [38]

2.13 The Cr-Si-Al ternary system

To date, there have been many investigations of phase equilibria in the Cr-Si-Al system. Liang et al. [40] used the CALPHAD method, Esslinger et al. [41] studied the Al rich corner of the system and confirmed that the composition of the τ_1 phase is $Al_{13}Cr_4Si_4$. The ternary compound β (AlCrSi) that was reported by Pratt et al. [42] was confirmed to be solid solution of Al in the binary silicide $CrSi_2$. Gupta [10] published isothermal sections at 800, 900, 1000 and 1100 °C over the entire composition range of the system. The ternary compound τ_1 was reported to exist only below 710 °C. Subsequently, Chen et al. [43] reported a new ternary phase τ_3 $(Al,Si)_{11}Cr_4$ which is isostructural with Mn_4Al_{11}. Their work focused on the isothermal section at 800 °C and confirmed the stability of three ternary compounds τ_1 ($Al_{13}Cr_4Si_4$), τ_2 (Al_9Cr_3Si) and τ_3 $(Al,Si)_{11}Cr_4$ at 800 °C. Raghavan [44] summarized this ternary system in two isothermal sections at 800 and 1100 °C. The ternary reactions in the Cr-Si-Al system are shown in Figure 2.14.

The microstructures of studied alloys revealed [10] the presence of a ternary intermetallic α that crystallized in the liquid as dendrites and was observed in association with the $CrAl_4$, $CrAl_7$ and Al solid solution. The α phase had precipitated in the liquid as a result of a number of quasi-peritectic, peritectic and eutectic reactions. A new quasi-peritectic reaction, designated as U_0 in Figure 2.14, at a temperature between 680 and 710 ^oC was proposed. The peritectic reaction $L + CrSi_2 + Cr_2Al_{11} \rightarrow \alpha$ at 710 ^oC, suggested by an earlier investigation, was modified with the $CrAl_4$ intermetallic replacing Cr_2Al_{11}. The $CrSi_2$ intermetallic was observed to have a high solubility of up to 20 at.% Al, which replaces the Si atoms in the lattice. The Cr_4Al_9 and Cr_5Al_8 intermetallics were observed to form as solid layer over Cr. Both these phases were observed in association with the Cr_5Si_3 silicide, suggesting the presence of $Cr_4Al_9 + Cr_5Si_3$, $Cr_5Al_8 + Cr_5Si_3$ and $Cr_4Al_9 + Cr_5Al_8 + Cr_5Si_3$ phase fields in the ternary phase diagram. The isothermal sections at 800, 1000 and 1100 ^oC are shown in Figure 2.15 [10].

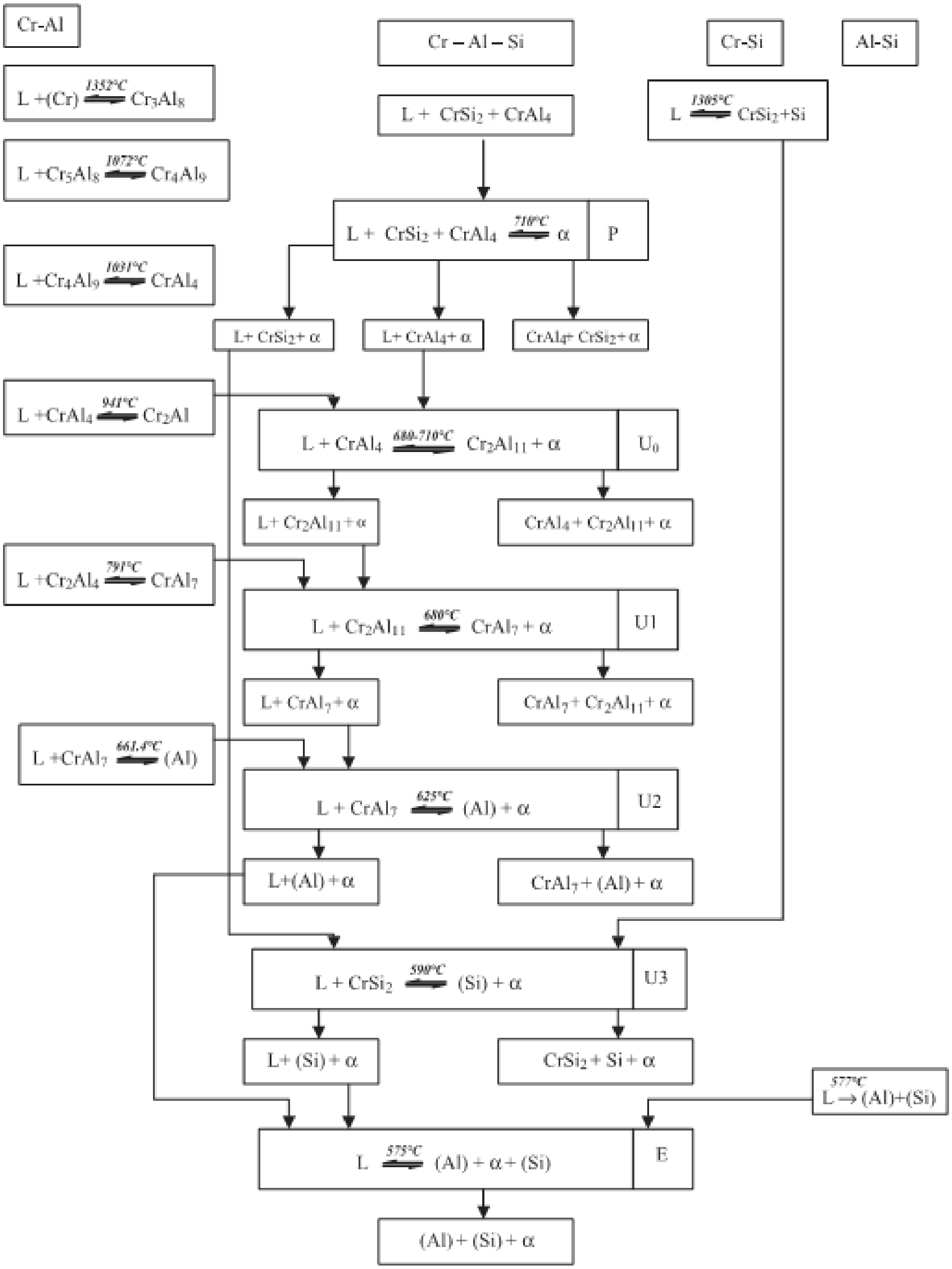

Figure 2.14 Ternary reactions in the Cr-Si-Al system [10]

(a)

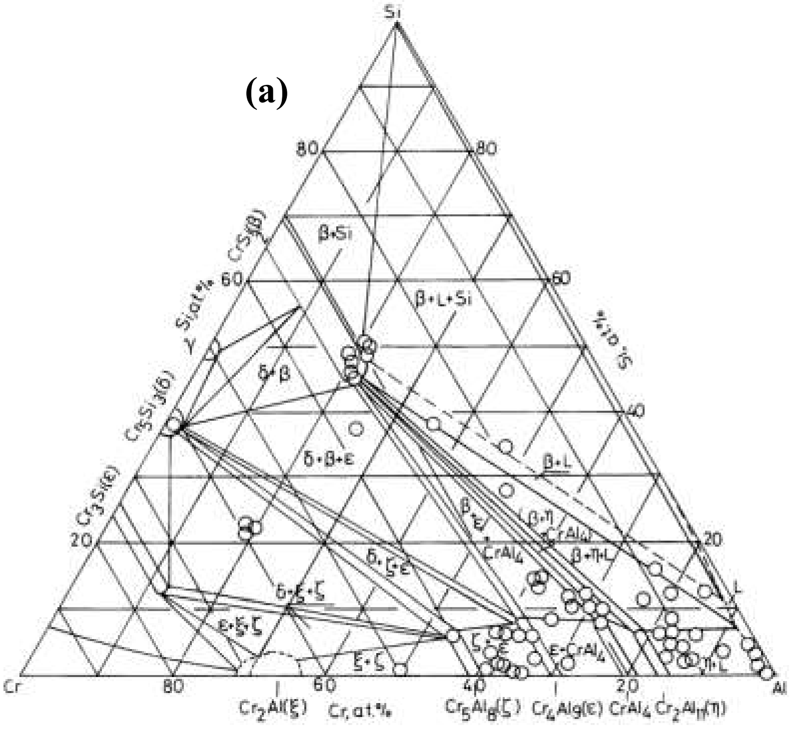

Si
80
80
CrSi2(β)
β+Si
60
60
Si, at %
β+L+Si
Si, at %
γ
δ+β
Cr5Si3(δ)
40
δ+β+ε
Cr3Si(ε)
β+L
β+ε
(β+π)
CrAl4
CrAl4
β+π+L
20
20
δ+ζ+ε
δ+ξ+ζ
L
ε+ξ+ζ
ζ
ε
ε+CrAl4
ξ+ζ
π+L
Cr
80
60
40
20
Al
Cr2Al(ξ)
Cr, at.%
Cr5Al8(ζ)
Cr4Al9(ε)
CrAl4
Cr2Al11(π)

(b)

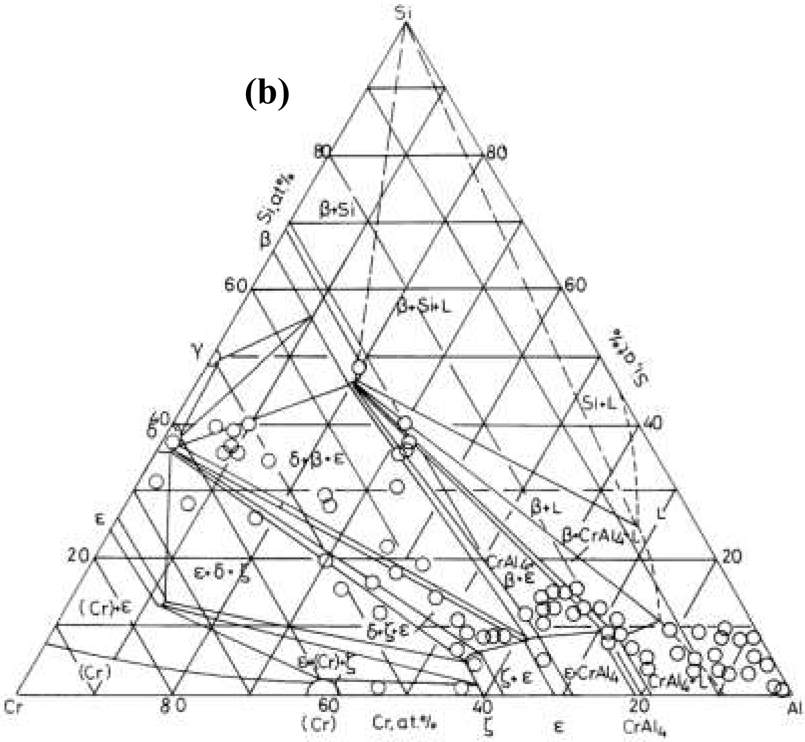

Si
80
80
Si, at %
β+Si
β
60
60
β+Si+L
Si, at %
γ
Si+L
δ
40
δ+β+ε
ε
β+L
L
β+CrAl4+L
CrAl4
β+ε
20
ε+δ+ξ
20
(Cr)+ε
δ+ζ+ε
ε+(Cr)+ξ
(Cr)
ζ+ε
ε+CrAl4
CrAl4+L
Cr
80
60
40
20
Al
(Cr)
Cr, at.%
ζ
ε
CrAl4

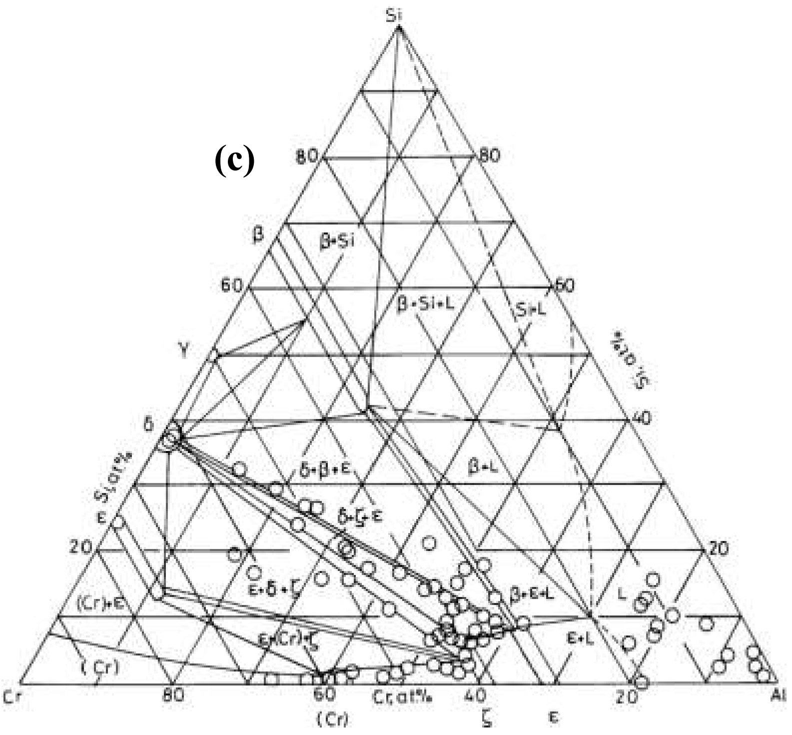

Figure 2.15 Isothermal sections of Cr-Si-Al at (a) 800, (b) 1000 and (c) 1100 ^{o}C [10]

2.14 The Cr-Si-Hf ternary system

Schoonover et al. [45] did a comprehensive investigation to provide experimental support for a thermodynamic model of the Cr and Hf rich ends of the equilibrium Cr–Hf-Si liquidus projection. The calculated Cr-Hf-Si liquidus projection is presented in Figure 2.16 overlaid with the alloy compositions investigated. The 1200 ^{o}C isothermal section is shown in Figure 2.17. The calculated invariant reactions in this system are listed in Table 2-2. Schoonover et al. [45] reported that a ternary eutectic reaction L → Cr_2Hf (HT) + Hf_2Si + β-(Hf) at approximately Hf–33Cr–3Si resulted to a morphology of Hf_2Si laths with a matrix of lamellar (Hf) + Cr_2Hf (HT). A ternary eutectic reaction L → Cr_3Si + (Cr) + Cr_2Hf (HT) led to a lamellar structure of (Cr), Cr_3Si and Cr_2Hf (HT) in the Cr-rich end at approximately Hf–73Cr–9Si. This was different from the ternary eutectic reaction of L → Cr_3Si + (Cr) + $(Cr,Hf)_5Si_3$ that was predicted at that composition by thermodynamic modeling. The ternary phase CrHfSi was found to be the primary phase in an alloy with composition in the $(Cr,Hf)_5Si_3$ region of the predicted liquidus projection. The compositional range of the CrHfSi primary phase region is not known [45].

Table 2-2 Invariant reactions in Cr–Hf–Si liquidus projection [18, 45]

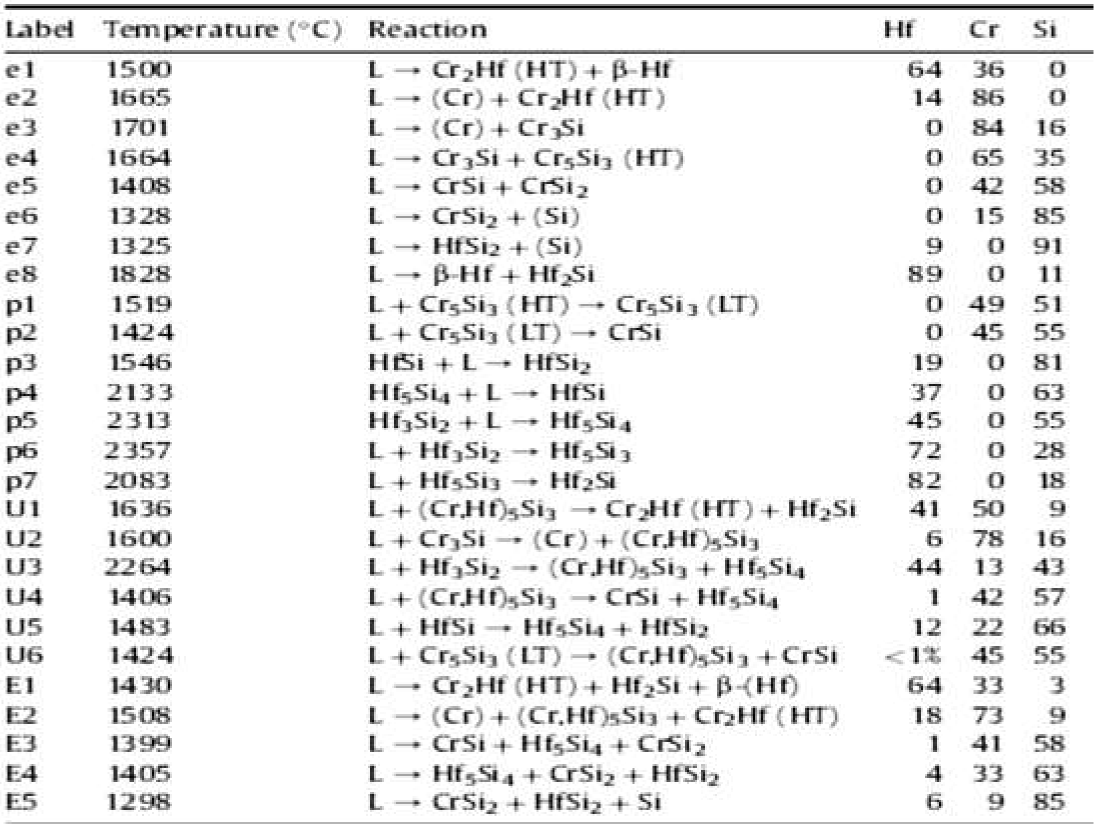

Label	Temperature (°C)	Reaction	Hf	Cr	Si
e1	1500	L → Cr_2Hf (HT) + β-Hf	64	36	0
e2	1665	L → (Cr) + Cr_2Hf (HT)	14	86	0
e3	1701	L → (Cr) + Cr_3Si	0	84	16
e4	1664	L → Cr_3Si + Cr_5Si_3 (HT)	0	65	35
e5	1408	L → CrSi + $CrSi_2$	0	42	58
e6	1328	L → $CrSi_2$ + (Si)	0	15	85
e7	1325	L → $HfSi_2$ + (Si)	9	0	91
e8	1828	L → β-Hf + Hf_2Si	89	0	11
p1	1519	L + Cr_5Si_3 (HT) → Cr_5Si_3 (LT)	0	49	51
p2	1424	L + Cr_5Si_3 (LT) → CrSi	0	45	55
p3	1546	HfSi + L → $HfSi_2$	19	0	81
p4	2133	Hf_5Si_4 + L → HfSi	37	0	63
p5	2313	Hf_3Si_2 + L → Hf_5Si_4	45	0	55
p6	2357	L + Hf_3Si_2 → Hf_5Si_3	72	0	28
p7	2083	L + Hf_5Si_3 → Hf_2Si	82	0	18
U1	1636	L + $(Cr,Hf)_5Si_3$ → Cr_2Hf (HT) + Hf_2Si	41	50	9
U2	1600	L + Cr_3Si → (Cr) + $(Cr,Hf)_5Si_3$	6	78	16
U3	2264	L + Hf_3Si_2 → $(Cr,Hf)_5Si_3$ + Hf_5Si_4	44	13	43
U4	1406	L + $(Cr,Hf)_5Si_3$ → CrSi + Hf_5Si_4	1	42	57
U5	1483	L + HfSi → Hf_5Si_4 + $HfSi_2$	12	22	66
U6	1424	L + Cr_5Si_3 (LT) → $(Cr,Hf)_5Si_3$ + CrSi	$<1\%$	45	55
E1	1430	L → Cr_2Hf (HT) + Hf_2Si + β-(Hf)	64	33	3
E2	1508	L → (Cr) + $(Cr,Hf)_5Si_3$ + Cr_2Hf (HT)	18	73	9
E3	1399	L → CrSi + Hf_5Si_4 + $CrSi_2$	1	41	58
E4	1405	L → Hf_5Si_4 + $CrSi_2$ + $HfSi_2$	4	33	63
E5	1298	L → $CrSi_2$ + $HfSi_2$ + Si	6	9	85

Table 2-3 Crystal structures of the intermetallic compounds in the Hf-Si binary system [30]

Phase	Pearson symbol	Space group	Prototype
α Hf	cI2	$Im\bar{3}m$	W
β Hf	hP2	$P6_3/mmc$	Mg
Hf_2Si	tI12	I4/mcm	Al_2Cu
Hf_5Si_3	hP16	$P6_3/mcm$	Mn_5Si_3
Hf_3Si_2	tP10	P4/mbm	Si_2U_3
Hf_5Si_4	tP36	$P4_12_12$	Si_4Zr_5
HfSi	oP8	Pnma	FeB
$HfSi_2$	oC12	Cmcm	ZrSi2
(Si)	cF8	$Fd\bar{3}m$	C(diamond)

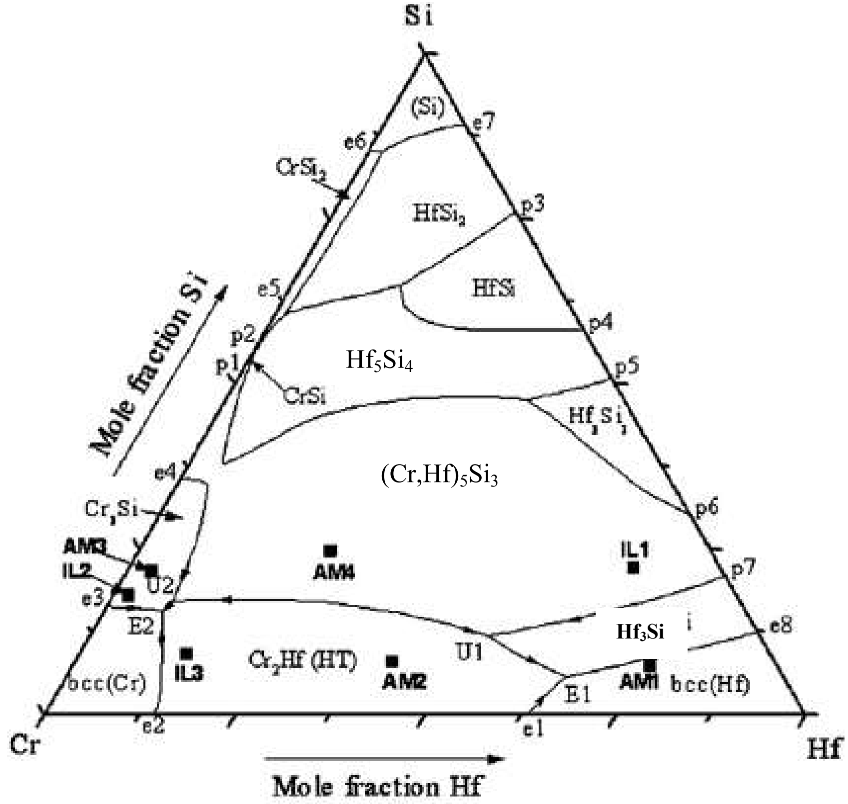

Figure 2.16 Liquidus projection of the Cr-Si-Hf system [18]

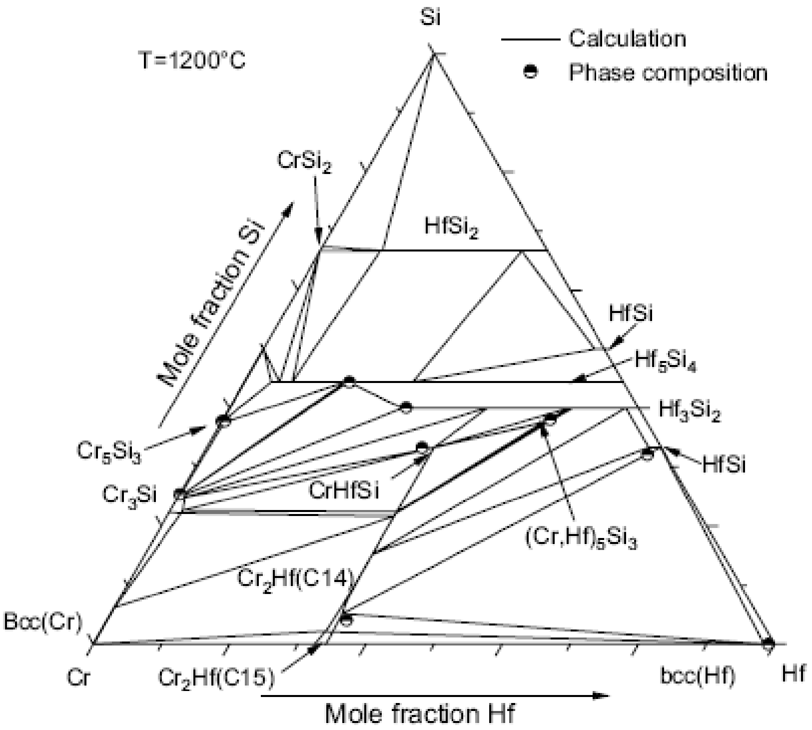

Figure 2.17 Isothermal section of the Cr-Si-Hf system at 1200 ˚C [18]

2.15 The Cr-Si-Ti ternary system

The phase equilibria in the Cr-Si-Ti system has been the subject to several investigations. Nowotny et al. [46] measured the mutual solubility between $TiSi_2$ and $CrSi_2$ at 1300 ^oC. Hallais et al. [47] found a ternary phase $T(Cr,Ti)_6Si_5$ with 11 to 41 at. % Ti content. The crystal structure of this phase was originally given as Ti_6Sn_5 - type (Immm, oI44) but subsequently corrected to Ti_6Ge_5-type (Ibam, oI44). Steinmetz [48] et al. reported the lattice parameters of the T –phase at the compositions $(Ti_{0.5}Cr_{0.5})_6Si_5$ and $(Ti_{0.6}Cr_{0.4})_6Si_5$. The ternary phase T was treated as a line compound $(Cr,Ti)_6Si_5$ with constant Si content in view of the crystal structure data and the composition range of Ti/Cr ratio where this phase was found to be homogeneous. In the 1000 ^oC isothermal section of the Ti-Cr-Si system (Figure 2.18(a)) constructed by Lysenko et al. [49] no TiCrSi phase exists. The solubility of Cr in both bcc (Ti) and Ti_5Si_3 is very high, 45 at. % and 23 (at. %) respectively, which means Cr is a stabilizer of these phases. On the other hand, the small solubility of Cr in the Ti_3Si phase indicates that Cr additions do not favour the existence of this phase. Du and Schuster [21] determined the isothermal sections at 800 ^oC and 1000 ^oC as well as liquidus lines in the Cr-Si-Ti system. Figure 2.18 (b) shows the corresponding liquidus projection, indicating that the composition for congruent melting of $\beta(Cr1\text{-}xTix)_5Si_3$ is far inside the ternary. The melting point of the Ti_5Si_3 was found to be above 2200 ^oC. Crystallographic data for the Cr-Ti-Si intermetallic compounds is listed in the Table 2-4.

Table 2-4 Crystallography data for the intermetallics in the Cr-Si-Ti system [21]

Phase	Lattice parameter (A^o)
$TiSi_2$	a=8.267, b=8.551, c=4.800
Ti_5Si_3	a=7.444, c=5.143
$CrSi_2$	a=4.430, c=6.365
αCr_5Si_3	a=9.150, c=4.639
Cr_3Si	a=4.555
$\beta TiCr_2$	a=4.932, c=8.005

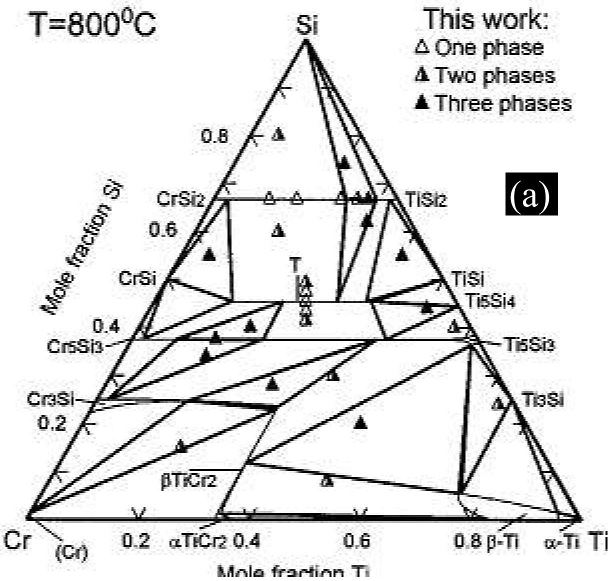
T=800⁰C
Si
This work:
△ One phase
Two phases
▲ Three phases
(a)
0.8
CrSi2
TiSi2
0.6
Mole fraction Si
CrSi
T
TiSi
Ti5Si4
0.4
Cr5Si3
Ti5Si3
Cr3Si
Ti3Si
0.2
βTiCr2
Cr
(Cr)
0.2
αTiCr2 0.4
0.6
0.8 β-Ti
α-Ti
Ti
Mole fraction Ti

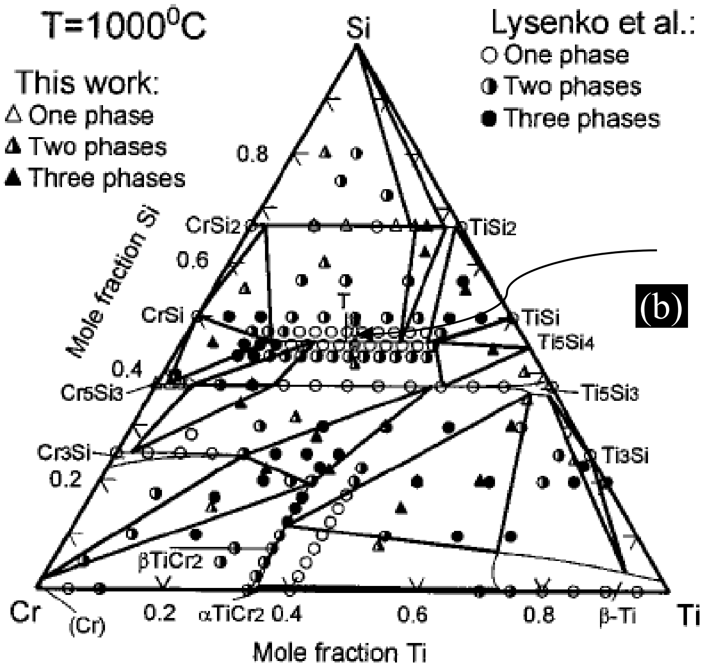
T=1000⁰C
Si
Lysenko et al.:
○ One phase
◑ Two phases
● Three phases
This work:
△ One phase
Two phases
▲ Three phases
0.8
CrSi2
TiSi2
0.6
Mole fraction Si
(b)
CrSi
T
TiSi
Ti5Si4
0.4
Cr5Si3
Ti5Si3
Cr3Si
Ti3Si
0.2
βTiCr2
Cr
(Cr)
0.2
αTiCr2 0.4
0.6
0.8
β-Ti
Ti
Mole fraction Ti

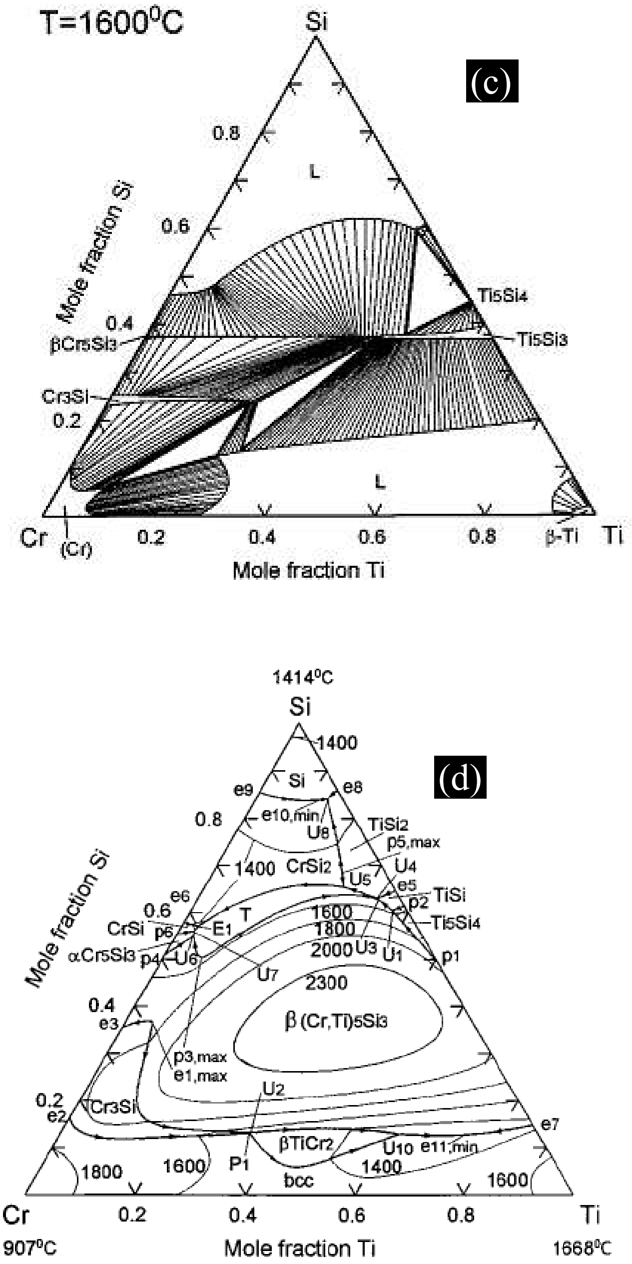

Figure 2.18 Isothermal sections (a) at 800 °C, (b) at 1000 °C, (c) at 1600 °C and (d) liquidus projection of the Cr-Si-Ti system [21]

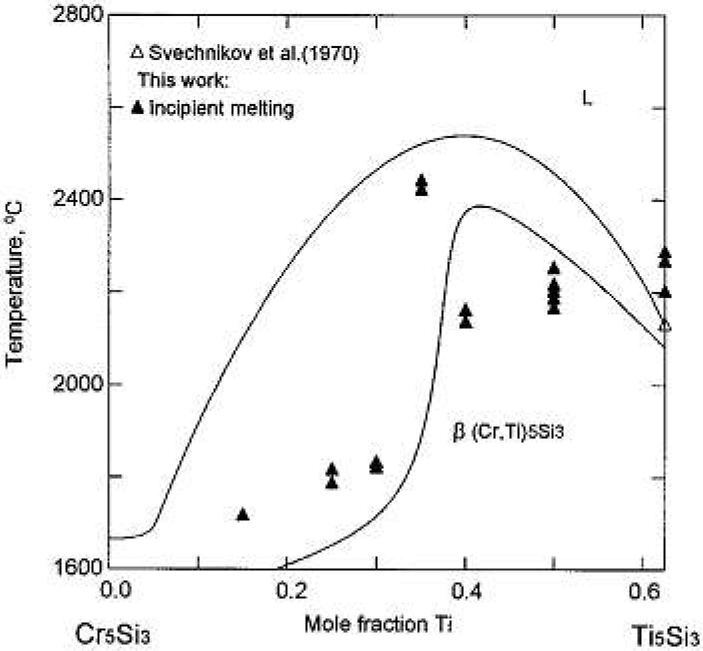

Figure 2.19 Calculated isopleth from Cr_5Si_3 to Ti_5Si_3 with the measured incipient melting points [21]

2.16 The Cr-Si-Nb ternary system

Goldschmit and Brand [50] determined an isothermal section of the Nb-Si-Cr ternary diagram at 1000 ˚C (Figure 2.18). According to this isothermal section three phase equiblirium exists among the Nb solid solution, the αNb_5Si_3 and ρ-phase. The ρ-phase is a ternary compound that has similar structural characteristics with the C14-Cr_2Nb Laves phase (Table 2-5); it is a hexagonal hp12 Laves phase of $MgZn_2$ type, with lattice parameter a=4.89 A^o and c=7.99 A^o. This C14 ternary phase begins to replace the C15-Cr_2Nb at silicon content as low as 2.5 at% and has considerable solubility for all three primary elements. Another point of interest in this system is the presence of both αNb_5Si_3 and βNb_5Si_3. Crystal structure data for intermetallics in the Cr-Si-Nb system is given in Table 2-5. It should be noted that in this table the αCr_5Si_3 is of the W_5Si_3 type.

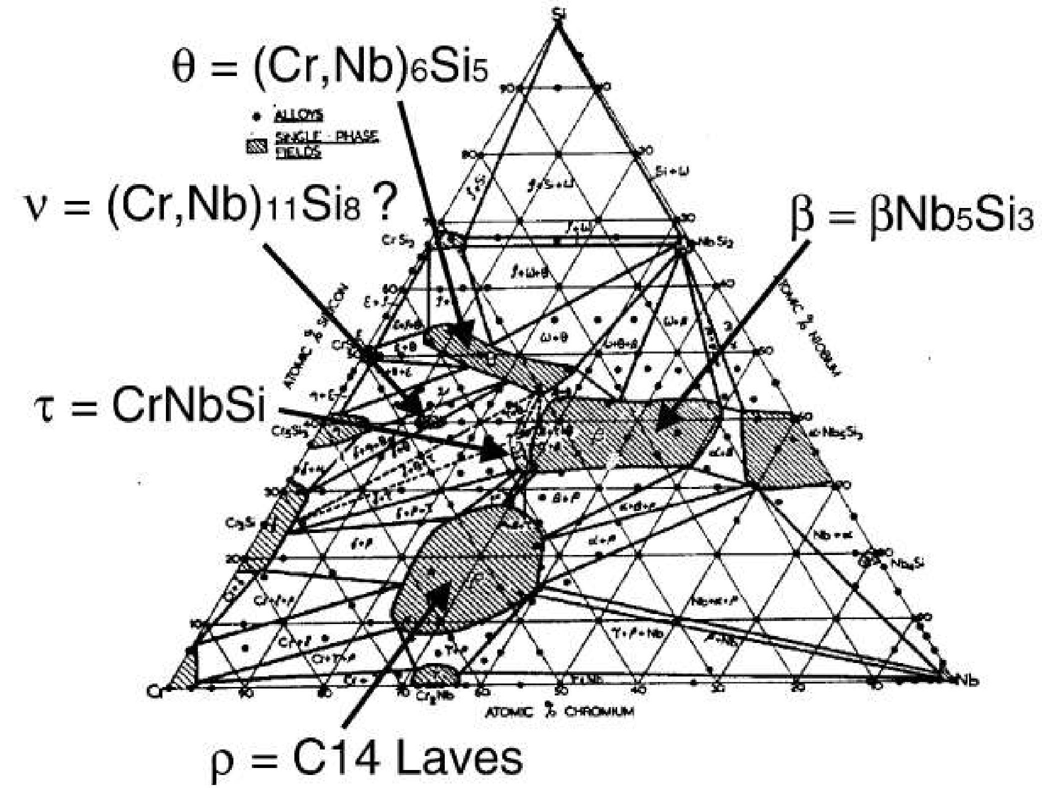

Figure 2.20 Isothermal section of the Nb-Si-Cr ternary system at 1000 ˚C [50]

Isothermal sections of the Nb-Cr-Si system (Figure 2.22, Figure 2.23) have been determined using diffusion multiples of high purity Nb, Cr, Si pieces, which were loaded into HIP cans made of commercial purity Ti and electron beam welded (Figure 2.21). Firstly, HIP was performed at 1204 ^{o}C and 200 MPa for 4 h , and then annealing at 1200 ^{o}C for 1000 h, 1150 ^{o}C for 2000 h, 1100 ^{o}C for 4000 h and 1000 ^{o}C for 4000 h. From the 1150 ^{o}C isothermal section of the Nb-Cr-Si system (Figure 2.23) obtained using this method it can be seen that at 1150 ^{o}C the Cr solubility in the bcc Nb and Nb_5Si_3 is ~ 3 at. % and 10 at. %, respectively [53].

Laves phases are not in equilibrium with bcc Nb and Nb_5Si_3 in the ternary system in Figure 2.23 . In composites processed at high temperatures (cast or directionally solidified (DS)), the C14-Laves phase was observed to co-exist with bcc (Nb) and Nb_5Si_3. According to thermodynamic modelling of the Cr-Nb-Si system by Shao [51], the Nb solid solution cannot be in direct equilibrium with the ternary CrNbSi phase, but it can coexist with the C14 Laves phase and the αNb_5Si_3. The diffusion multiple approach used by Zhao et al. [52] was based on the basis of local equilibrium at interfacial regions and is quite efficient, but the resultant data should be verified with other approaches. This is quite important, especially if it is considered that on some occasions, due to unclear reasons, one of the equilibrium phases cannot be formed by inter-diffusion reaction [53].

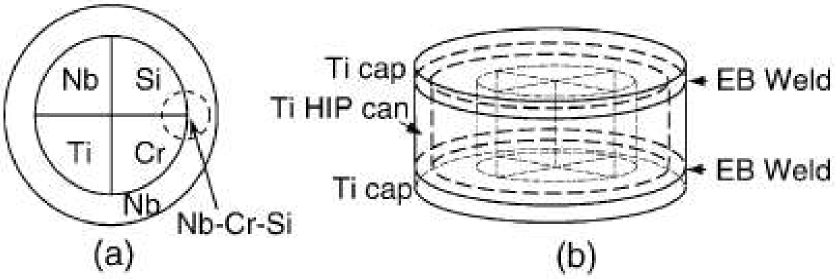

Figure 2.21 schematic diagrams of diffusion multiple for the Nb–Cr–Si ternary system: (a) cross-sectional view; and (b) perspective view [53].

Table 2-5 Crystal structure data for the Nb-Cr-Si ternary system [53]

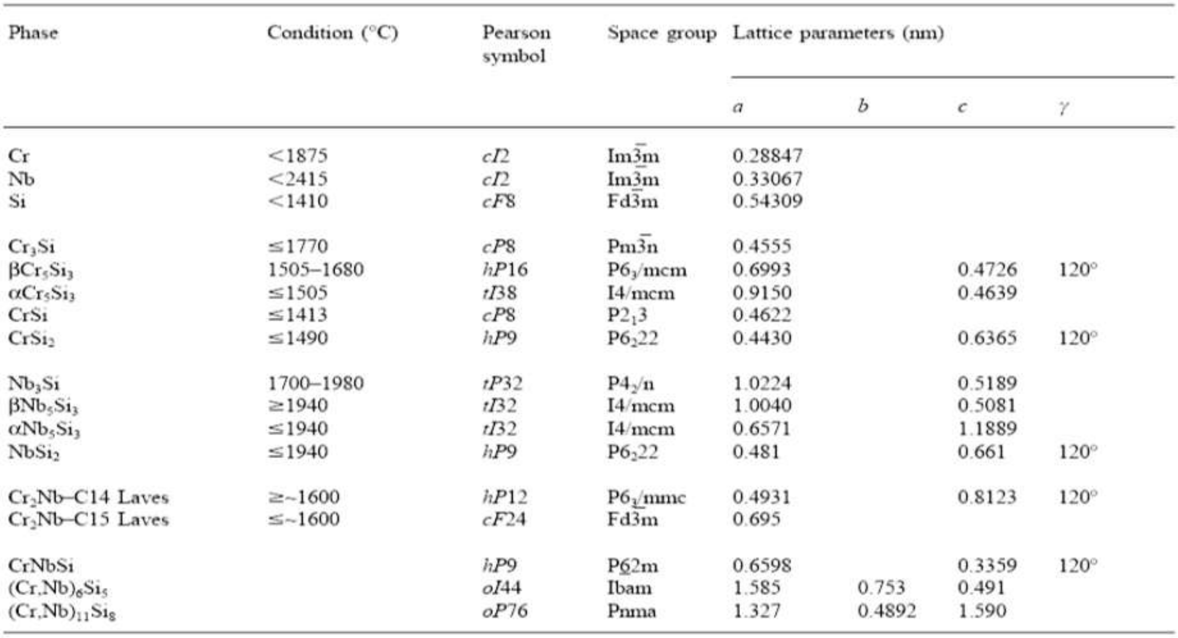

Phase	Condition (°C)	Pearson symbol	Space group	Lattice parameters (nm)			
				a	*b*	*c*	γ
Cr	<1875	*cI2*	$Im\bar{3}m$	0.28847			
Nb	<2415	*cI2*	$Im\bar{3}m$	0.33067			
Si	<1410	*cF8*	$Fd\bar{3}m$	0.54309			
Cr_3Si	≤1770	*cP8*	$Pm\bar{3}n$	0.4555			
βCr_5Si_3	1505–1680	*hP16*	$P6_3/mcm$	0.6993		0.4726	120°
αCr_5Si_3	≤1505	*tI38*	$I4/mcm$	0.9150		0.4639	
CrSi	≤1413	*cP8*	$P2_13$	0.4622			
$CrSi_2$	≤1490	*hP9*	$P6_222$	0.4430		0.6365	120°
Nb_3Si	1700–1980	*tP32*	$P4_2/n$	1.0224		0.5189	
βNb_5Si_3	≥1940	*tI32*	$I4/mcm$	1.0040		0.5081	
αNb_5Si_3	≤1940	*tI32*	$I4/mcm$	0.6571		1.1889	
$NbSi_2$	≤1940	*hP9*	$P6_222$	0.481		0.661	120°
Cr_2Nb–C14 Laves	≥~1600	*hP12*	$P6_3/mmc$	0.4931		0.8123	120°
Cr_2Nb–C15 Laves	≤~1600	*cF24*	$Fd\bar{3}m$	0.695			
CrNbSi		*hP9*	$P\bar{6}2m$	0.6598		0.3359	120°
$(Cr,Nb)_6Si_5$		*oI44*	Ibam	1.585	0.753	0.491	
$(Cr,Nb)_{11}Si_8$		*oP76*	Pnma	1.327	0.4892	1.590	

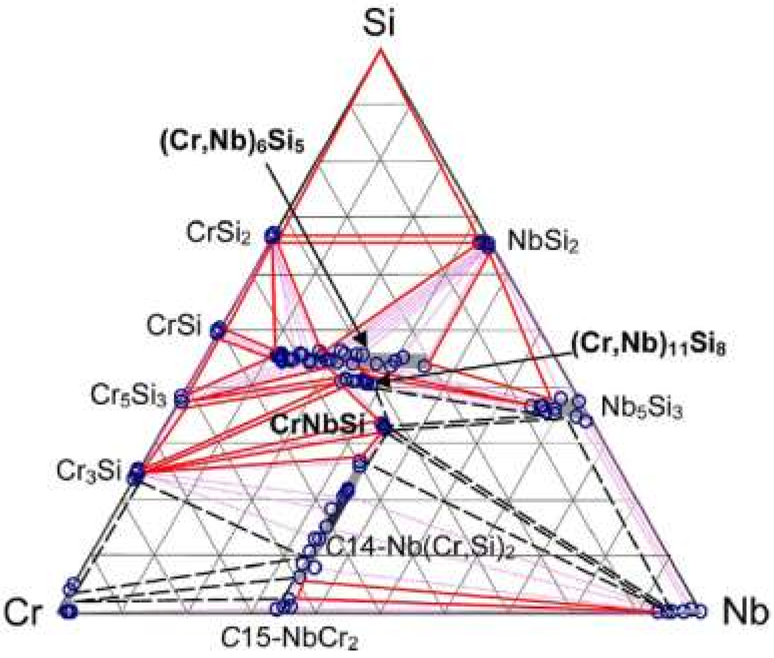

Figure 2.22 The 1000 °C isothermal section of the Nb–Cr–Si system obtained from the tri-junction area of the diffusion multiple annealed at 1000 °C for 4000 h [53].

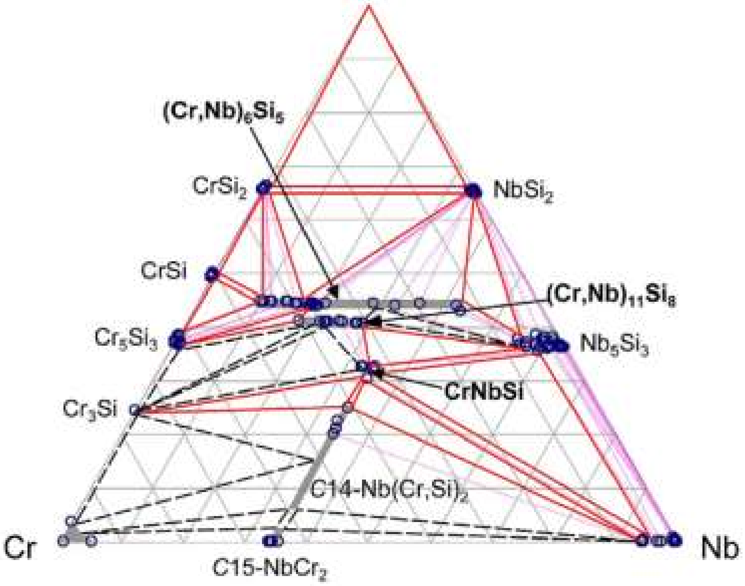

Figure 2.23 The 1150 °C isothermal section of the Nb–Cr–Si system obtained from the tri-junction area of the diffusion multiple annealed at 1150 °C for 2000 h [53].

Similar to the Nb-Cr-Si ternary, the existence of TM_6Si_5 is also reported in Cr-Si-M ternaries (M: transition metal, Ta, Hf, Ti). The crystal structure data for TM_6Si_5 is shown in Table 2-6.

Table 2-6 Crystal structure data for TM_6Si_5 phases [21, 54]

phase	Pearson symbol	Space group	Lattice parameters(A^o)
Nb_6Si_5	oI44	Ibam	a=15.85, b=7.53, c=4.91
Hf_6Si_5	oI44	Ibam	a=7.60, b=16.10, c=4.96
Ti_6Si_5	oI44	Ibam	a=7.49, b=15.92, c=4.87
Ta_6Si_5	oI44	Ibam	a=7.50, b=15.96, c=4.85

2.17 Summary

According to the binary and ternary phase diagrams reviewed the following remarks can be made.

The Cr-Si-Al phase equlibria data suggest that in Al poor alloys the $CrSi_2$, CrSi and Cr_5Si_3 silicide can be in equilibrium while in Al rich alloys, the Al_8Cr_5, Cr_3Si and Cr_5Si_3 can be in equilibrium. There is significant solid solubility of Al in $CrSi_2$ but not in CrSi and Cr_5Si_3. The Al_8Cr_5 is the Al-Cr intermetallic, which is stable up to 1350 ^oC, the βNb_5Si_3 is isomorphous with Cr_5Si_3 but not the Ti_5Si_3 and Hf_5Si_3.

In the binary Ti-Si, Hf-Si and Nb-Si systems there are no 6-5 silicides whereas with the addition of Cr in the ternaries the 6-5 silicide can form. Thus, it is possible to select Al poor and Al rich Cr-Si-Al base alloys in the microstructure of which it should be possible to form Si and Al rich intermetallic phases.

3. Oxidation of Intermetallics

The oxidation behaviour of intermetallic compounds has been studied by many researchers. In this chapter, the selective oxidation of intermetallic compounds will be studied and compared with that of Ni and Fe-based alloys. The fundamentals of selective oxidation, described in Figure 3.1, apply to intermetallic compounds as they do to alloys. However, there have been some discrepancies in the quantitative data [55-58]. A comprehensive study of oxygen solubilities in intermetallic compounds shows that most intermetallics have negligible oxygen solubility. Thus, internal oxidation is rarely observed in intermetallic compounds except Ti_3Al and Ni_3Al, which dissolve substantial amounts of oxygen.

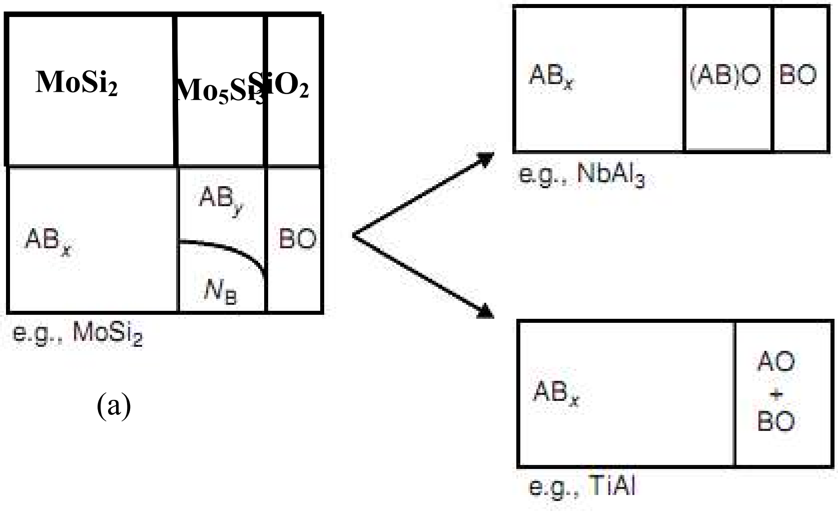

(b)

(a)

(c)

Figure 3.1 Schematic diagram showing the special features associated with the oxidation of intermetallic compounds with limited homogeneity ranges (N_B: solute concentration) [57].

The compound stoichiometry is of great importance in its oxidation behaviour. Most intermetallic compounds exist over only narrow ranges of composition, for example see Figures

2.1, 2.2, 2.8, 2.11. Thus can form a lower intermetallic compound beneath the oxide by the selective oxidation of one component from the compound. Therefore, the properties of a lower compound play a key role in maintaining the growth of the protective oxide scale. It is reported that some compounds such as Mo_5Si_3 provide enough flux of Si atoms to the oxide-alloy interface to form a silica scale on $MoSi_2$. For many intermetallics such as $NbAl_3$, the lower compound formation in the microstructure has negative effect on the formation of a continuous oxide scale on the surface. During the early stages of exposure of this compound a continuous alumina layer forms but the outward diffusion of Al causes the formation of the lower aluminide Nb_2Al beneath the oxide. Unlike the primary compound, Nb_2Al is not able to form continuous alumina scale and the latter spalls off and then reforms beneath the Nb_2Al layer and then wraps it [58-60]. The repetition of this process leads to the formation of a layered Nb-Al oxide scale.

The relative stability of oxide is also a key factor when an alloying component e.g. Al, Si is required to form alumina or silica that are more stable than the oxides of any other component formed in the alloy. For instance, Nb or Ti-based compounds form oxides of the base metal that are as nearly stable as those of Al or Si (Figure 3.2). For some of these compounds, e.g. Ti based compounds, a two phase scale of intermixed alumina and titania is reported to be stable. The prevailing metal activity must be taken into account for the determination of oxide stability.

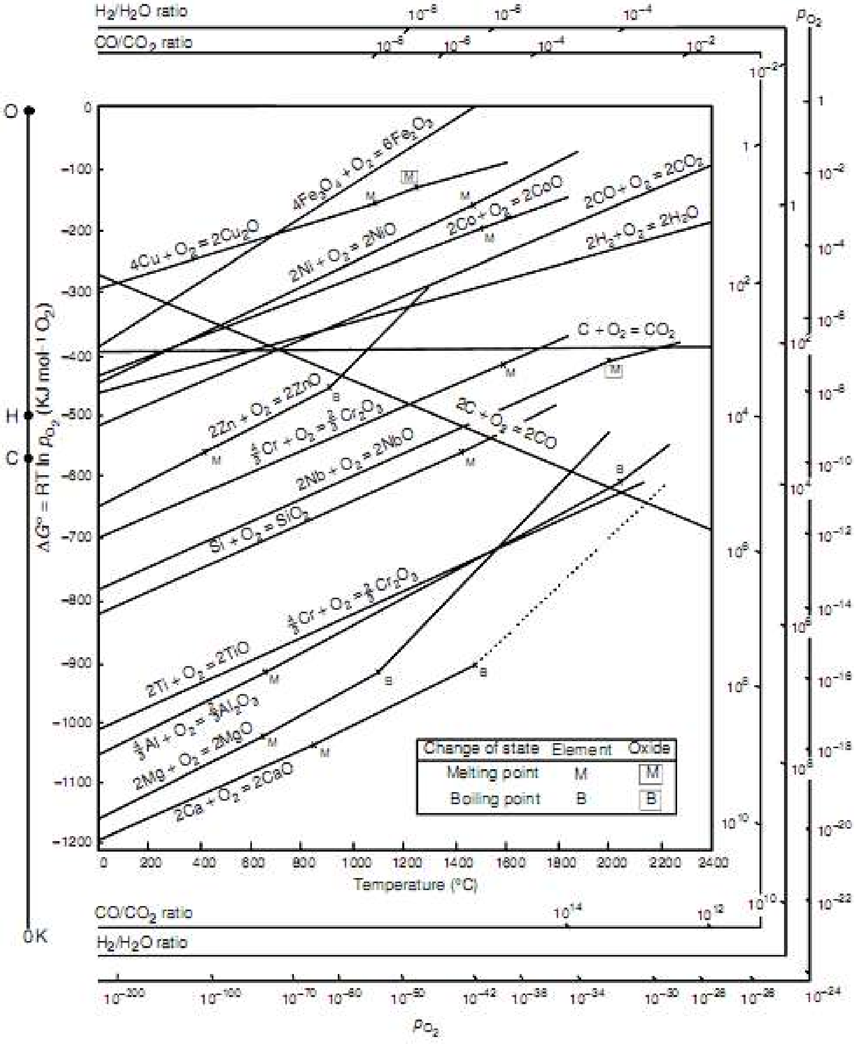

Figure 3.2 Standard energy of formation of selected oxides as a function of temperature (Ellingham diagram) [57].

3.1 Oxidation of refractory metals and their alloys

In general, the refractory metals (Nb,Ta,Mo,Re and W) form oxides that have lower melting point than that of the metal. The usage of refractory metals at high temperatures is thus difficult because of their poor oxidation resistance. As shown in Figure 3.3, the oxidation rates of Nb are high and limit its use compared with Ni. However, alloying has beneficial effect on the mechanical properties and the oxidation resistance of refractory metals that make them potential candidates for high temperature structural applications, such as rockets and reentry systems as well as high efficiency power plant turbines [61]

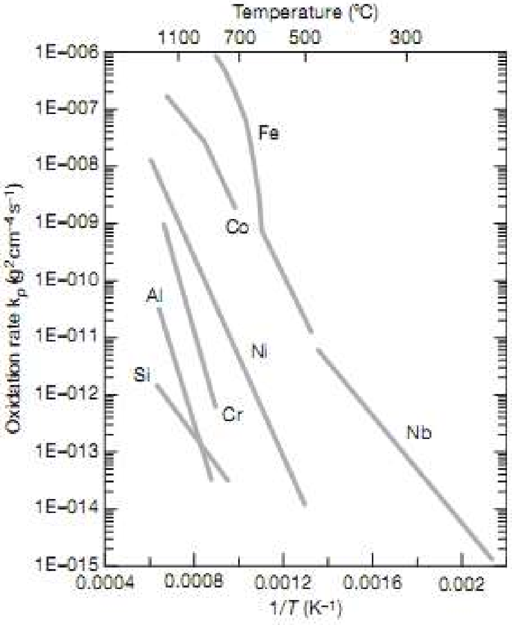

Figure 3.3 Summary of parabolic oxidation rate constants for some of metals [61]

Due to the high oxygen solubility in refractory metals, many oxides can form in a range of temperatures and oxygen partial pressures as oxidation products. This makes the oxidation of refractory metals more complicated than that of Fe, Ni, and Co. The equilibrium vapour pressures of some refractory metal oxides at pO_2 =1 atm are summarized in Figure 3.4.

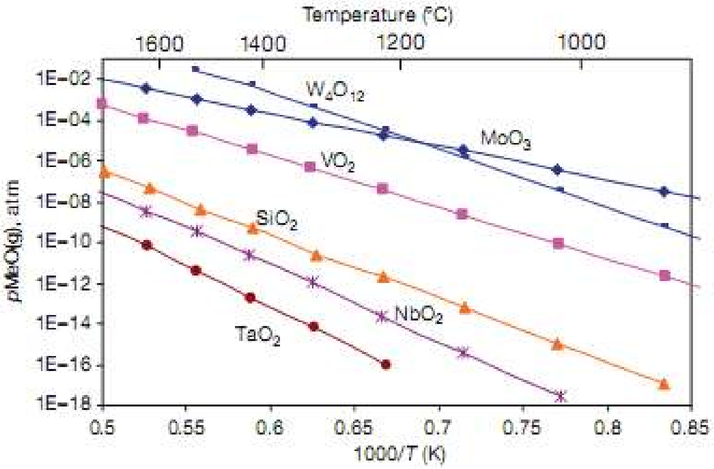

Figure 3.4 Equilibrium vapour pressure of some refractory metal oxides and silicon dioxide at pO_2=1atm. Reproduced by Hou [61] from Ramberg et al.

The oxidation mechanism of refractory metals and alloys has been studied before 1970. The effect of W addition on Ta oxidation was studied. Nb-Hf and Nb-Zr alloys were also studied. It was reported that the Hf or Zr addition does not have superior beneficial effect on the oxidation of Nb alloys. Instead, internal oxides of Hf and Zr formed with detrimental effect on the mechanical properties of the alloys such as embrittlement. It is reported that the oxidation of Nb in air was decreased between 800 and 1000 ^oC by transition metal alloying (Hf, Zr, W, Mo, Ti or Ta). However, the Nb alloys in service-required coatings for further protection [61].

Nb-Al based alloys can form a protective alumina scale in air at 1400-1600 ^oC if (i) Al solubility lies between 37.5 to 50 at.%, (ii) the addition of Ti increases the solubility and diffusivity of Al and (iii) the addition of Cr and/or V decreases the solubility and diffusivity of O in the alloy. It was reported that the alloy 25.4Nb-29.1Ti-2.8Cr3.5V-39.2Al (wt%) formed a protective alumina scale in air above 1000 ^oC and was stable up to 1400 ^oC and the oxidation kinetics of this alloy was close to that of NiAl [62]. The oxidation resistance of Nb-Al-Ti-V-Cr alloys has been improved by adding dispersions of alumina and yttria particles that are thermally and chemically stable in the Nb alloys matrix [63].

Despite research efforts, development of high temperature refractory metal-based alloys that can form a protective oxide scale has not yet been achieved. Considering that the alloying element addition usually leads to detrimental effects in at least one property of the alloy [61, 64], coatings are essential for refractory metal-based alloys. This will be discussed below.

3.1.1 Coatings on refractory metals and alloys for oxidation protection

In general, a coating can be applied to an alloy surface as an external layer, or be formed in the alloy surface region as a single/multi-layer. Such coatings have been reported to improve the oxidation resistance of refractory metal alloys [65]. It has been reported that $MoSi_2$ and $NbSi_2$ either unalloyed or alloyed with Fe and Cr, and aluminides are very efficient coatings [66, 67]. Despite the oxidation protection offered by these coatings, the latter are very brittle. Thus, crack formation due to the thermal expansion coefficient mismatch with the substrate is highly likely. Even after considering noticeable improvements compared with the uncoated alloys, the coated systems cannot be used yet reliably in service owing to lack of durability. Therefore, research is needed to optimize the coating by designing multi component multi-layer coatings, rather than single layer coatings. Moreover, the deposition technique and surface treatment are of great importance for the durability and lifetime of coating systems [12, 61, 64].

3.2 Oxidation of silica-forming alloys

Pure silica (SiO_2) is one of the most impermeable oxides at high temperatures. The low activation energy for the diffusion of oxygen in SiO_2 makes the latter a more protective oxide scale than alumina at temperatures above ~ 1080 °C. It is reported that the silica forming alloys are suffering from the formation of volatile SiO in the environments where the oxygen activity is very low [68]. The Si addition has been limited to a small amount similar to Al addition as it has negative effect on mechanical properties of Fe, Co, and Ni based alloys. The research has shown that the Cr addition can considerably increase the formation of silica, where a silica layer is formed under either a Cr_2O_3 healing layer or an external Cr_2O_3 layer. The type of silica formed at the oxide-alloy interface (continuous or intermittent) is dependent not only on the Si concentration but also on the oxidation time and temperature. An amorphous silica forms for T

≤ 1000 ^{o}C [69], whereas at 1100 ^{o}C depending on alloy composition and oxidation time, the crystalline silica is stable in the scale in the form of either cristobalite or tridimite [70].

3.2.1 Silicides

For many high-temperature aerospace applications, alloys of the refractory metals Mo, Nb, and Ta can provide suitable properties for use as structural materials. Due to their high melting points and low densities, refractory metal alloys have long been considered for high temperature applications, but their use as high temperature structural components in service has been limited by inferior oxidation behaviour [71, 72]. Coatings based on silicides of refractory metals have been the most common materials used to protect refractory metals from oxidation at high temperatures [73]. Ceramics such as Yb_2SiO_4, Si_3N_4 and yttria stabilized HfO_2have also been considered although it is not likely to be adequate bonding to refractory metal substrates for broad use as a means of protection from oxidation [61].

Apart from protective silica formed on the silicides, the silicides should also have enough oxidation resistance by themselves. There are many Si rich M_xSi_y silicides (M = Ti, V, Nb, Cr, Mo, W) that are capable of forming protective silica layers at $T > 900$ ^{o}C [74]. However, the kinetics of oxidation is the key factor for the development of a protective silica scale. The higher temperature and longer oxidation exposures are also important in forming a silica layer. For instance, $MoSi_2$ can form silica at $T > 1000$ ^{o}C, whereas portions of the surface were covered by MoO_3 at lower temperatures [75]. Brady et al. [73] studied the high temperature oxidation of many silicides, namely $MoSi_2$, Mo_5Si_3, $TiSi_2$, Ti_5Si_3, V_5Si_3, Cr_3Si and Fe and Ni silicides with a focus on Mo and Ti silicides.

Pesting is often a problem with intermetallics. Pest oxidation has been most extensively studied on the $MoSi_2$, where it disintegrates the silicide to powder and/or fragments at temperatures between 300 and 550 ^{o}C [73]. It is reported that the alloy response to pesting is dependent on the microstructure and stoichiometry of its phase precursors [76-79]. For instance, Mo concentration for Mo/Si ratio higher than 0.5 can increase pesting of the alloy but the pesting decreased by increasing the Si solubility in $MoSi_2$ [80].

There has been significant volume of research focused on alloys of the ternary Mo-Si-B system in order to achieve a better oxidation resistance at high temperatures [81-83]. Several alloy compositions were able to form a protective borosilicate glass at high temperatures. It is reported that the viscosity of the protective glass can be decreased by increasing of the B/Si ratio [84, 85].

The studies by Samsonov et al.[86] and Nowak [87] on the oxidation behaviour of $CrSi_2$ showed unsatisfactory behaviour whereas Grabke and Brumm [88, 89] reported work on the oxidation behaviour of $CrSi_2$ where this silicide can be used similarly to $MoSi_2$ at high temperatures. A good oxidation resistance could be expected of this phase since its two elements, which form slow-growing oxide scales are coupled. As the vapour pressures of the higher chromium oxides are rather high (Figure 3.5 b), it might be expected that at rather high temperatures, chromium evaporates upon oxidation and silicon forms a vitreous protective silica layer. At high oxygen pressures the evaporation of silicon is negligible since the oxide with the highest vapour pressure is silicon monoxide for which the vapour pressure decreases with increasing oxygen pressure (Figure 3.5 a).

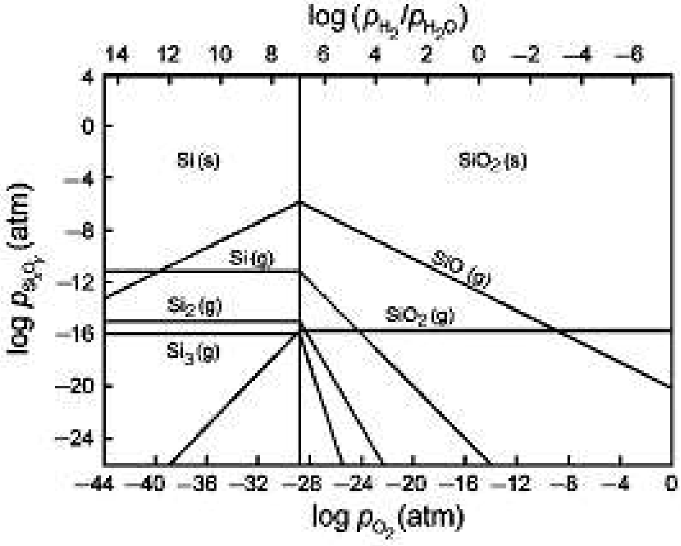

(a)

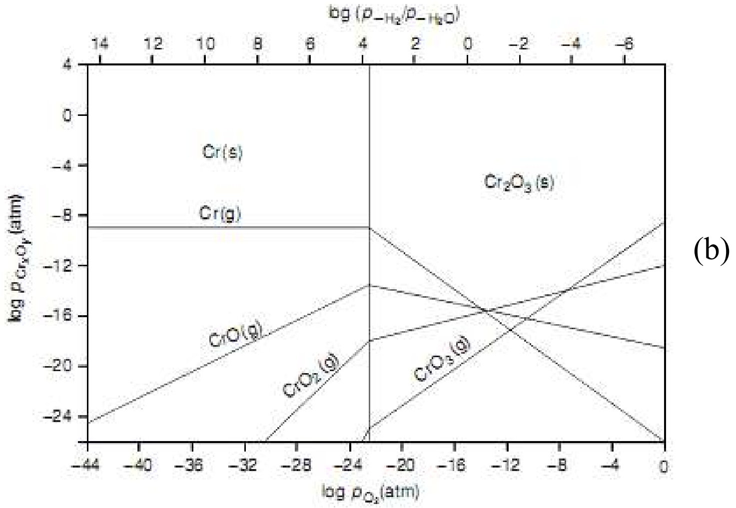

Figure 3.5 Vapour pressures at 977 °C versus oxygen pressure, (a) silicon and silicon oxide and (b) chromium and chromium oxides [57]

According to Grabke and Brumm [88], $CrSi_2$ oxidizes with formation of a Cr_2O_3 scale in the temperature range 900 °C to 1050 °C. Despite the fact that the Cr activity is very low and silicon activity and concentration are very high on and in the silicide, no selective oxidation of Si was found. The parabolic rate constant of the Cr_2O_3 growth was relatively low, owing to the low chromium activity at the $CrSi_2/Cr_2O_3$ interface. At temperatures $\geq$ 1200 °C, the oxidation was very fast and linearly time dependent. No protective layer was formed but a very convoluted layer composed of both oxides, an inner layer of SiO_2 and an outer layer of Cr_2O_3. These layers were coherent but their adherence to the substrate was very weak [88, 89].

The effectiveness of silicide coatings largely depends upon their ability to maintain passive oxidation behaviour in temperatures and environments where the underlying refractory metal would otherwise exhibit active oxidation. The oxides formed by silicide coatings on niobium substrates have been shown to depend on both coating composition and temperatures. Unalloyed coating slurry powder (e.g. containing only silicon) applied using the slurry coating process form $NbSi_2$ after the coating diffusion treatment. Upon exposure to air, SiO_2 and Nb_2O_5 form, and the coating evolves into a mixture of $NbSi_2$ and Nb_5Si_3. The unalloyed coating exhibits pest oxidation. Alloying the coatings with chromium results in the formation of $NbSi_2$

and $(Nb,Cr)_5Si_3$ after the coating diffusion treatment. The oxide products include Nb_2O_5, Cr_2O_3, SiO_2, and $CrNbO_4$. Pest oxidation is also observed [61, 90].

3.3 Oxidation of alumina-forming alloys

Two types of commercial Al_2O_3-forming alloys has been developed: (i) the aluminides, such as FeAl and NiAl, and (ii) the MCrAl type alloys that are often used with superalloys, where 'M' represents the base metal and can be a mixture of Fe, Ni, and Co [61].

There must be a minimum aluminum concentration in the aluminides that makes them cable of forming a protective Al_2O_3. For instance, at least ~ 19 at. % Al is needed to achieve the selective oxidation of Al to develop a protective Al_2O_3 scale and suppress the oxidation and growth of iron oxides [91, 92]. For the NiAl aluminide, the minimum Al concentration is higher than that of FeAl, at ~22 at. %, where a healing layer of alumina forms at the scale alloy interface and the outer surface of the scale consisted of NiO and/or $NiAl_2O_4$. It is also reported that the minimum Al solubility essential to form protective alumina layer decreased to 10 at.% by adding of 18-20 at.% Cr in MCrAl type alloy. Moreover, the scale adhesion can be enhanced by adding of Ti, Zr, Hf, Y, or via their synergy [93].

The alumina can form in various forms depending on temperature and time of oxidation. The cubic θ or γ phase or a mixture of the two form upon heating and α alumina nucleates later at the alumina alloy interface [94-96]. It is reported that the latter develops very fast in an alloy at higher temperature and in the presence of Cr and/or Fe [97-99], but additions of Hf, Y or Zr can slow down the development of α alumina. [61, 99-101].

In general, the formation of alumina scales follows parabolic kinetics, indicating diffusion-controlled growth. It is reported that the growth rate of θ alumina is faster than that of α alumina [102]. This is why the oxidation kinetics consisted of two parabolic stages with different activation energies. Hindam and Whittle [103] studied the parabolic rate constant of the alloys containing reactive element (RE) and concluded that the contributions from transitional alumina phases were not always eliminated and must be taken into account [61,103].

In order to better correlate alloy composition to oxidation rates, Hou [61] re-evaluated the data given by Hindam and Whittle together with the data for Ni-, Fe- or Pt-based alloys, shown in Figure 3.6. According to the Figure 3.6, the growth rates of α alumina scales can vary more than 2 times from 1000 to 1300 or 1400 ^{o}C with average activation energy of scale formation of about 240 kJmol^{-1} [61, 103-105]. This Figure will be used to compare the results of this study with the Ni-, Fe- or Pt-based alloys.

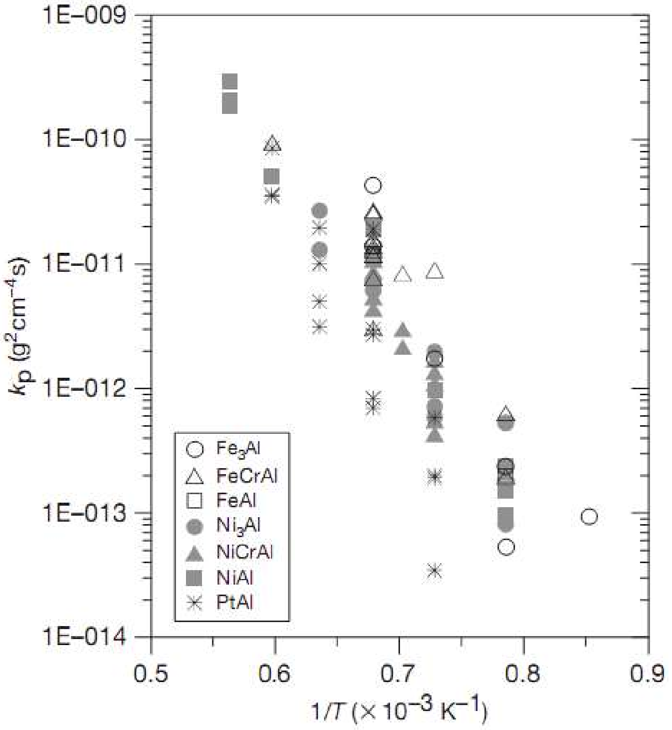

Figure 3.6 Parabolic rate constants showing the Al_2O_3 scale growth rate on different Fe,Ni, and Pt-based alloys [61].

Reactive elements have a beneficial effect on selective oxidation by decreasing the Cr and Al solubility in the alloy that is needed to form the protective alumina. However, if the alloy has enough amounts of Cr or Al, the RE addition (eg. Y) only can decrease the exposure time needed for these scales to be established [104]. It is also reported that RE addition or its oxides can greatly increase diffusion of Cr by supplying many nucleation sites to promote the formation of the oxide layer [106, 107].

4. Experimental procedure

4.1 Materials

The nominal compositions of the alloys were Cr-(45-X)Si-(5+X)Al-5M where X=0 or 20 and M is the transition metal Hf, Ti and Nb. All compositions in this thesis are given in atomic percent unless indicated otherwise. The alloys were prepared using commercial purity materials (Cr 99.99 wt%, Si 99.99 wt.%, and Al 99.9 wt.% , Hf 99.8 wt.%, Nb 99.9 wt. % and Ti 99.9 wt.%).

As discussed in section 2.17,the selection of the alloy compositions was based on considerations of forming silicon and aluminium rich intermetallics to form silica, alumina and chromia protective scales or a mixture of them as multicomponent scales (e.g. Mullite ($3Al_2O_32SiO_2$), Spinel). The nominal compositions of the alloys studied are listed in Table 4-1.

Table 4-1 Nominal compositions (at. %) of Cr-Si based intermetallic alloys of this study

Alloy Code	Cr	Si	Al	Hf	Ti	Nb
AN1	45	45	5	5	---	---
AN2	45	25	25	5	---	---
AN3	45	45	5	---	5	---
AN4	45	25	25	---	5	---
AN5	45	45	5	---	---	5
AN6	45	25	25	---	---	5

4.2 Ingot preparation

The alloy ingot buttons were prepared by arc melting using a non-consumable tungsten electrode in a water-cooled copper crucible under argon atmosphere. The melting chamber was evacuated to 10^{-3} Pa, in which argon was introduced to 50 kPa before arc melting. A pure Ti specimen was melted as an oxygen getter prior to alloy melting. A voltage of 50 V and current of 600 A were used in this work. The alloy was re-melted five times to ensure homogeneity of its button. Weight losses after arc melting were $\leq$ 0.5 wt%.

4.3 Specimen preparation

In order to study the microstructure and oxidation behaviour of the alloys, different specimen preparation techniques were used.

4.3.1 Scanning electron microscopy samples

Cross-sections perpendicular to the bottom of the ingot were used for phase identification, backscatter electron imaging, chemical composition analysis and hardness testing. The specimens were sectioned using an Isomet D5000 sectioning machine, mounted in conducting bakelite, ground with 400, 800 and 1200 grit SiC grinding papers, and then polished to a 1µm finish using diamond paste. All specimens were ultrasonically cleaned with isopropanol for 10 minutes. The samples used for EBSD were additionally polished using a mixture of colloidal silica and hydrogen peroxide.

4.3.2 XRD samples

The ingots were crushed using brass mortar and pestle. The coarse powder was then grinded in ceramic mortar and pestle to get fine powder. The powders were then sieved to get very fine powder for XRD sample. The size of the latter powders was 20-60 µm.

4.3.3 Oxidation samples

Cubic samples, 3x3x3 mm^3 in dimension were cut from the as cast alloys, and their surfaces were ground to 1200 grit. The samples were ultrasonically cleaned before oxidation experiment. The dimension of each sample was measured using a micrometer and optical microscope and the surface area was calculated.

4.4 XRD analysis

The X-ray diffraction (XRD) technique was used to examine the phases present in the as cast and heat-treated alloys. Phase analysis for the thin oxide scales formed on the oxidized samples after exposure at 800, 1000 and 1200 ^{o}C was performed with Glancing Angle X-Ray Diffraction (GAXRD). Phase identification was done by comparing the measured d-spacing values with those in JCPDS (Joint Committee of Powder Diffraction Standards) cards.

4.4.1 Bragg-Brentano geometry

A Siemens D500 X-ray diffractometer was used to examine the phases present in each alloy. The $CuK\alpha$ ($\lambda = 1.540562$ Å) radiation source of the diffractometer was excited by an acceleration voltage of 40 kV and a current of 30 mA. The sample rotation step of 0.02^0 and detector movement of 1^0(2θ.min) were applied in the experiments.

4.4.2 Glancing Angle XRD

A Siemens D5000 X-ray diffractometer with $CuK\alpha$ ($\lambda = 1.540562$ Å) radiation was used for glancing angle X-ray diffraction. The penetration depth of X-rays in the surface of the specimen depends on the incidence angle (glancing angle). The glancing angles used for oxidized samples were 2 ^{o}, 5^o, 7^o and 10^o.

4.5 Heat treatment

Isothermal heat treatments of the specimens, which were cut from the centre parts of the as cast ingots, were carried out at 1200 ^{o}C and 1300 ^{o}C for 100 hours in an argon atmosphere. Titanium sponge was placed in a ceramic boat in both sides of the heating tube. This was done due to presence of oxygen in the tube to suppress the oxidation of the specimens. The heating rate used was 3 ^{o}C /min. The samples were furnace cooled after isothermal heat treatment.

4.6 Scanning electron microscopy

Backscatter electron imaging was performed in a JEOL 6400 SEM. Quantitative chemical analysis for the as cast and heat-treated alloys was carried out in the JEOL 6400 equipped with Energy Dispersive X-ray Spectrometry (EDX) and INCA software. An accelerating voltage of 20 kV was used under which the electron beam size was about 1 micron. Calibration of the detector was repeated every hour using a pure Co standard, and the count rate for the calibration was controlled to be around 3000 cps by adjusting the probe current. High purity standards of Al, Cr, Si, Hf, Ti, Nb and Ta were used for the EDX analysis. The ZAF correction method (Z: atomic number, A: absorption, F: fluorescence) was used in the analysis. A number of 5 and 10 EDX analyses were done respectively for large area and individual phase. The large area analyses of the bulk were acquired at X300 Magnification. Due to the overlapping issues in the peaks of Hf Mα and Si Kα, the energy line of Hf Mα was changed to Lα line to get the actual Hf and Si content in the alloys. In the tables in chapter 5 to 7, data about the EDS analyses is given as the average values, the standard deviations, and the minimum and maximum analyses values.

Secondary electron imaging was carried out using an FEI Sirion 200 FEG SEM in order to study of the topography of the oxidized samples. The samples were placed in the aluminum stub using a conductive carbon sticker. The samples were coated with a thin carbon conductive layer to reduce the electron charge effect. Under accelerating voltage of 20 kV, the working distance (WD) and spot size were set ≤ 7 mm and three respectively.

4.6.1 Electron backscatter diffraction pattern

Electron Backscatter Diffraction (EBSD) analysis was performed on samples to aid phase identification. The pattern of Kikuchi lines on the phosphor screen camera is electronically digitized and processed to recognize the individual Kikuchi lines. These data are used to identify the phase, to index the patterns. These patterns are effectively projections of the geometry of the lattice planes in the crystal, and they give direct information about the crystalline structure and crystallographic orientation of the grain from which they originate. When used in conjunction with a data base that includes crystallographic structure information for phases of interest and with software for processing the EBSP's and indexing the lines, the data can be used to identify phases based on crystal structure. The equipment used was an FEI Sirion 200 FEG SEM equipped with an Oxford/HKL Channel 5 EBSD system. High quality EBSD patterns were recorded from each phase. Initial manual inspection of these patterns, and those from other regions of samples, confirmed the uniqueness of each phase. Subsequent semi-automated phase identification using the Channel 5 system indicated the best structural matches based on comparison with crystal structure and lattice parameter data presented in Table 4-2. The NIST crystal database was used to characterize different phases in samples. Standard crystal structure database was made using the Channel 5 Twist software for the phases that were not in the database. In EBSD phase solution, 7 bands were used to match a sphere to appropriate phases with a Mean Angular Deviation (MAD) fit of 0.2-0.4 degree. The atomic coordination and equivalent isotropic displacement parameter of $M_2Cr_4Si_5$ crystal used by Twist software is given in Table 4-3.

Table 4-2 Cell parameters for $M_2Cr_4Si_5$ (M=Ti, Nb, Hf, Zr) [52-54]

Compound	*a*(Å)	*b*(Å)	*c*(Å)
$Ti_2Cr_4Si_5$	7.496	15.92	4.878
$Nb_2Cr_4Si_5$	15.850	7.530	4.910
$Hf_2Cr_4Si_5$	7.608	16.103	4.967
$Zr_2Cr_4Si_5$	7.630	16.137	4.979

Table 4-3 Atomic coordination and equivalent isotropic displacement parameter for $M_2Cr_4Si_5$(M=Ti, Hf and Nb) [54]

Atom	Wyckoff position	x	y	z
M	8j	0.37874	0.34863	0
Cr1	8j	0.2529	0.06119	0
Cr2	8g	0	0.30889	0.25
Si1	8j	0.0736	0.43587	0
Si2	8j	0.2070	0.21121	0
Si3	4a	0	0	0.25

4.7 Hardness measurement

CV instruments Vickers hardness tester (model 430 AAT) was used to measure the Macrohardness of the alloy under load of 10 kg with a holding time of 30 s. Microhardness of precursor phases in the alloys was measured using a Mitutoyo (model) hardness machine under load of 0.03 kg with a holding time of 15 s. A minimum of 10 Micro and Macro indentation test were carried out for each alloy/phase and the dimensions of indents were measured twice.

4.8 Differential scanning calorimetry

A Netzsch STA 449 F3 Jupiter differential scanning calorimeter (DSC) with the Pyris software package were used to assess the solidus temperature of each alloy. Small amount of powder of each alloy, weighing ~3 mg, was used for the analysis. The sample was placed an alumina cup into the furnace. An empty pan was placed into the furnace as a reference. The sample and reference pan were heated at a rate of 3 ^{o}C /min up to 1500 ^{o}C. The Pyris software monitored the heat flow in mW into the furnace and recorded any variations. Changes in state due to a phase melting and/or transformation were recorded on a temperature vs heat flow curve.

4.9 Thermo-gravimetric analysis

Thermo-gravimetric analysis (TGA) was carried out with a Netzsch STA 449 F3 Jupiter thermo-gravimetric analyzer at 800, 1000 and 1200 ^{o}C. Cubic samples were prepared as described in section 4.3.3. Cubic specimens were placed in a small alumina crucible positioned on the balance, and then the balance was calibrated to the initial total weight. The specimens were heated to the test temperature and were held at that temperature for 100 hours, then furnace cooled to ambient temperature after the isothermal oxidation. Both the heating and cooling rates used in the TG experiment were 3 ^{o}C/min. The weight gain versus time was recorded during isothermal oxidation experiment. The weight was normalized against the initial surface area of the specimen. The weight of the sample was also measured before and after TGA in order to verify weight change results. The oxide scales that formed after TG experiments were studied by glancing angle X-ray diffraction (see section 4.4.2).

4.10 Volume fraction measurement

The % area fraction of silicides and aluminides in the microstructures of the alloys was measured using the software KS Run 3.0 in a Polyvar Met optical microscope by uploading the SEM images of the alloys taken by JEOL 6400 SEM in the software. The SEM images of large areas (X300) of both as cast and heat-treated alloys that were used to make large area analyses in EDX were used to measure the area fraction. For each alloy condition, at least three SEM images were used and the average was calculated.

4.11 Density measurement

The density of the alloys was measured using Archimedes principle and a Sciteq digital precision balance, equipped with a density measurement kit. Density of each alloy was measured 10 times and the average value was calculated. The weight of each specimen was measured in air as well as in distilled water and having the density of the liquid in the lab temperature (20 ^{o}C), the calculation of the density was performed using the equation below:

$$\rho(alloy) = \frac{W\ air\ .\rho(liq)}{W\ air\ \ -W(liq)}$$

where ρ(alloy) is density of alloy , W(air) is weight of the alloy in air , W(liq) is weight of the alloy in liquid and ρ(liq) is density of the liquid (distilled water) .